Atmospheric
Chemistry
and Physics

Airborne investigation of black carbon interaction with low-level, persistent, mixed-phase clouds in the Arctic summer

Marco Zanatta[1,2], **Stephan Mertes**[3], **Olivier Jourdan**[4], **Regis Dupuy**[4], **Emma Järvinen**[2],
Martin Schnaiter[2], **Oliver Eppers**[5,6], **Johannes Schneider**[5], **Zsófia Juryányi**[1], and **Andreas Herber**[1]

[1]Section of Atmospheric Physics, Alfred-Wegener-Institut, Helmholtz-Zentrum für Polar- und
Meeresforschung (AWI), Bremerhaven, Germany
[2]Institute of Meteorology and Climate Research, Karlsruhe Institute of Technology, Karlsruhe, Germany
[3]Department of Atmospheric Microphysics, Leibniz-Institut für Troposphärenforschung, Leipzig, Germany
[4]Laboratoire de Météorologie Physique, Université Clermont Auvergne/OPGC/CNRS,
UMR 6016, Clermont-Ferrand, France
[5]Particle Chemistry Department, Max Planck Institute for Chemistry, Mainz, Germany
[6]Institute for Atmospheric Physics, University of Mainz, Mainz, Germany

Correspondence: Marco Zanatta (marco.zanatta@kit.edu)

Abstract. Aerosol–cloud interaction is considered one of the largest sources of uncertainty in radiative forcing estimations. To better understand the role of black carbon (BC) aerosol as a cloud nucleus and the impact of clouds on its vertical distribution in the Arctic, we report airborne in situ measurements of BC particles in the European Arctic near Svalbard during the "Arctic CLoud Observations Using airborne measurements during polar Day" (ACLOUD) campaign held in the summer of 2017. BC was measured with a single-particle soot photometer aboard the *Polar 6* research aircraft from the lowest atmospheric layer up to approximately 3500 m a.s.l (metres above sea level). During in-cloud flight transects, BC particles contained in liquid droplets (BC residuals) were sampled through a counterflow virtual impactor (CVI) inlet. Four flights, conducted in the presence of low-level, surface-coupled, inside-inversion, and mixed-phase clouds over sea ice, were selected to address the variability in BC above, below, and within the cloud layer. First, the increase in size and coating thickness of BC particles from the free troposphere to the cloud-dominated boundary layer confirmed that ground observations were not representative of upper atmospheric layers. Second, although only 1 % of liquid droplets contained a BC particle, the higher number concentration of BC residuals than BC particles sampled below cloud indicated that the totality of below-cloud BC was activated by nucleation scavenging but also that alternative scavenging processes such as the activation of free-tropospheric BC at the cloud top might occur. Third, the efficient exchange of aerosol particles at cloud bottom was confirmed by the similarity of the size distribution of BC residuals and BC particles sampled below cloud. Last, the increase in the BC residual number concentration (+31 %) and geometric mean diameter (+38 %) from the cloud top to the cloud bottom and the absolute enrichment in larger BC residuals compared with outside of the cloud supported the hypothesis of concomitant scavenging mechanisms but also suggested the formation of BC agglomerates caused by cloud processing. The vertical evolution of BC properties from inside the cloud and below the cloud indicated an efficient aerosol exchange at cloud bottom, which might include activation, cloud processing, and sub-cloud release of processed BC agglomerates. In the case of persistent low-level Arctic clouds, this cycle may reiterate multiple times, adding an additional degree of complexity to the understanding of cloud processing of BC particles in the Arctic.

1   Introduction

It is well known that clouds strongly affect the surface energy budget in the Arctic (Shupe and Intrieri, 2004; Lubin and Vogelmann, 2006). However, the interaction between aerosol particles and clouds remains one of the major sources of uncertainty in radiative forcing estimations in the Arctic and on a global scale (Bellouin et al., 2020; IPCC, 2021).

Black carbon (BC) particles are carbonaceous aerosol particles emitted by the incomplete combustion of fossil fuels and biomasses (Bond et al., 2004); due to their unique absorption of solar radiation in the visible spectrum, they play an important role in the Arctic radiative balance. First, BC particles directly interact with solar radiation, causing a net warming of the local atmospheric layer (Flanner, 2013). Second, the change in local temperature might influence the vertical distribution of clouds via semi-direct effects (Sand et al., 2013). Third, via aerosol–cloud interaction, also known as the first indirect effect, BC activation might lead to a change in the microphysical properties of clouds, with consequences for cloud radiative properties (Sand et al., 2013). Lastly, after deposition, BC can decrease the snow albedo, promoting melting via the snow darkening effect (Flanner et al., 2009). All of these processes are strongly interconnected (Quinn et al., 2015), making BC the second strongest atmospheric Arctic warmer after carbon dioxide (Oshima et al., 2020).

The seasonality in the BC concentration at the Arctic surface is characterized by a maximum in early spring and a minimum in summer (Quinn et al., 2015). A similar seasonality was recently reported on the vertical scale (Juirányi et al., 2023). Given the rarity of BC sources within the Arctic, most of the BC mass reaches the Arctic via long-range transport (Xu et al., 2017). Hence, the seasonal cycle is primarily controlled by the circulation of air masses between the Arctic and southern latitudes (Bozem et al., 2019) and by precipitation events during long-range transport (Croft et al., 2016). Therefore, the ability to understand how BC interacts with clouds (cloud scavenging) is crucial for quantifying the BC burden and radiative forcing in the Arctic region. Overall, cloud scavenging is responsible for 90 % of BC mass deposition in the Arctic (Dou and Xiao, 2016), with the highest precipitation rate in summer contributing to the decline in the BC burden from late spring to autumn (Garrett et al., 2011; Mori et al., 2020). Moreover, cloud scavenging influences the vertical distribution of BC in the atmosphere, with convective precipitation controlling the concentration of BC in the upper troposphere and stratiform precipitation controlling the concentration of BC at the surface (Mahmood et al., 2016). However, the complexity of in-cloud and below-cloud scavenging of BC limits the ability of global models to reproduce the temporal, vertical, and horizontal distribution of BC in the entire Arctic region (Whaley et al., 2022) and, con-

sequently, the radiative forcing of BC (Samset et al., 2013, 2018).

The ability of BC particles to promote droplet formation (hygroscopicity) is one of the most complex parameterizations in global model schemes (Holopainen et al., 2020). In fact, the cloud nucleation ability of BC depends on fundamental particle properties, such as diameter and mixing state, which evolve during atmospheric ageing due to condensation and coagulation processes. While fresh BC particles are not hygroscopic, aged BC particles show an increase in hygroscopicity (Schwarz et al., 2015; Ohata et al., 2016) correlated with the particle diameter (Motos et al., 2019a) and the formation of inorganic and organic coatings (Dalirian et al., 2018; Motos et al., 2019b). Although considerable progress has been made with respect to the quantification of BC hygroscopicity, its ability to act as an ice-nucleating particle is more uncertain. Despite the lack of measurements, field and laboratory studies classify BC as a non-efficient ice-nucleating particle, at least at warm temperatures (Kupiszewski et al., 2016; Kanji et al., 2020).

Arctic-relevant processes add an extra level of complexity to the study of cloud scavenging of aerosol and BC particles in liquid and mixed-phase clouds. The nucleation scavenging of aerosol particles from the below-cloud layer represents the dominant activation mechanism in the Alaskan Arctic (Earle et al., 2011; McFarquhar et al., 2011). In contrast, Igel et al. (2017) showed that free-tropospheric aerosol particles may be activated at the top of low-level Arctic clouds protruding into the inversion layer (clouds within inversion; Sedlar et al., 2011), leading to downward transport of free-tropospheric aerosol particles into the boundary layer. Moreover, other in-cloud processes might compete with nucleation scavenging. In fact, interstitial BC particles (BC particles present in the cloud volume but not activated into cloud particles) may be efficiently captured by pre-existing cloud particles via interstitial scavenging (Baumgardner et al., 2008). Despite often being ignored, the number concentration of Arctic aerosol particles is highly sensitive to interstitial scavenging that occurs during long-range transport (Croft et al., 2016). Furthermore, cloud processes such as droplet coalescence, riming, and the Wegener–Bergeron–Findeisen (WBF) process modify the size (droplet coalescence and riming) and phase partitioning (riming: from liquid to ice; WBF: from liquid to interstitial) of activated aerosol particles (Ding et al., 2019). In the presence of persistent low-level Arctic clouds, aerosol particles may undergo the cloud processes described above several times. Solomon et al. (2015) identified a recycling mechanism for cloud-active aerosol particles that comprises activation at the cloud bottom, growth within the cloud, sedimentation, release below the cloud layer, and subsequent reactivation at the cloud bottom. Finally, understanding of the complex interaction between BC and clouds

in the Arctic is further complicated by the rarity of in situ observations, especially at the cloud level (Tørseth et al., 2019).

In this work, we present unprecedented vertically resolved airborne measurements of BC particles sampled inside and outside of clouds in the European Arctic in the summer of 2017 during the "Arctic CLoud Observations Using airborne measurements during polar Day" (ACLOUD) campaign (Wendisch et al., 2018, 2022). The objective is to provide the first insights into the BC–cloud interaction in the Arctic with a particular focus on (1) the presence and properties of cloud-active BC, (2) the scavenging mechanism of BC, and (3) the impact of cloud processing on the vertical distribution of BC.

2 Methodology

The ACLOUD campaign was conducted between 23 May and 26 June 2017 in the northwest region of Svalbard (Norway) within the framework of the "Arctic Amplification: Climate Relevant Atmospheric and Surface Processes and Feedback Mechanisms (AC)³" project (see https://www.ac3-tr.de/, last access: 12 July 2023; Wendisch et al., 2018, 2022). All validated data are published in the World Data Center PANGAEA as instrument-separated data subsets (https://doi.org/10.1594/PANGAEA.902603; Ehrlich et al., 2019). Flight operations and atmospheric measurements used in the present work are described in the following, and the instrumentation, measured parameters, and relative abbreviations are listed in Table 1.

2.1 Flight operations

Atmospheric observations were carried out with two research aircraft from the Alfred Wegener Institute (AWI): the *Polar 5* and the *Polar 6* (Wesche et al., 2016). The *Polar 5* was equipped with remote-sensing instruments, whereas the *Polar 6* was equipped with instrumentation to make in situ measurements. A full list of the deployed instrumentation can be found in Ehrlich et al. (2019). The present study contains the results of three distinct subsets of ACLOUD flights. The first subset included 12 flights that provided vertical measurements of aerosol and cloud particles up to an altitude of 3500 m a.s.l (metres above sea level). The flights were performed on 27 May 2017 and on 2, 4, 5, 8, 13, 14, 16, 17, 18, 23, and 26 June 2017 over open water, the marginal sea ice zone, and ground (Fig. 1a). The second subset was composed of four flights performed on 2, 4, 5, and 8 June 2017 with repeated sampling of low-level clouds over the marginal sea ice zone (Fig. 1b), thereby providing the best opportunity to investigate the interaction of BC with mixed-phase clouds in the boundary layer. The last subset was composed of one single flight performed on 25 June 2017, representing the sole case of clear-sky conditions (Fig. 1b).

2.2 Techniques

2.2.1 Meteorological measurements

Meteorological parameters such as pressure (P), relative humidity (RH), and temperature (T) were recorded at a 1 Hz resolution with the basic meteorological sensor suite of *Polar 6*, which has been fully described in previous works (Herber et al., 2012; Schulz et al., 2019; Ehrlich et al., 2019). T and RH data were merged with aircraft position and air pressure into a 1 Hz basic meteorological dataset (https://doi.org/10.1594/PANGAEA.902849; Hartmann et al., 2019). The potential temperature (T_P) was calculated from measured ambient temperature (T) and pressure (P) as follows: $T_P = T \ (P_0/P)^{0.286}$.

2.2.2 Cloud particle measurements

The Small Ice Detector Mark 3 (SID-3; Hirst et al., 2001; Vochezer et al., 2016) was operated aboard *Polar 6* to measure the cloud particle number size distribution in the 5–45 μm diameter range (https://doi.org/10.1594/PANGAEA.960269, Järvinen and Schnaiter, 2023). Liquid droplets and ice crystals were distinguished based on the two-dimensional (2-D) scattering patterns for the particle sphericity, as described in Vochezer et al. (2016). More details on the data processing of the SID-3, including the correction of coincidence artefacts, can be found in Järvinen et al. (2023). Based on the phase discrimination, we calculated the number concentration of liquid droplets (N_{Dro}), from which the liquid water content (LWC) was estimated assuming spherical particles and a particle density of 1 g cm⁻³.

The cloud imaging probe (CIP, Droplet Measurement Technologies – DMT, Longmont, CO, USA; Baumgardner et al., 2001) allows for the quantification of the dimension and shape of cloud particles and was used to derive the number concentration of non-spherical ice crystals (N_{Ice}; calculated according to circularity, as in Crosier et al., 2011) and the ice water content (IWC; calculated using the mass–diameter relationship defined by Brown and Francis, 1995). The number size distribution of ice crystals presented in this work is based on effective equivalent diameter, which is more comparable to previous Arctic measurements (Mioche et al., 2017). Due to the significant uncertainties in the probe's sensitive area for the smallest particle sizes, the nominal detection size range was reduced to 75–1550 μm in the present work. The mass fraction of ice water (IWF) was calculated from the IWC estimated by the CIP and the LWC estimated by the SID-3. The properties of the ice crystals derived from CIP measurements performed aboard the *Polar 6* are published in the PANGAEA database (https://doi.org/10.1594/PANGAEA.899074; Dupuy et al., 2019).

The Airborne Mobile Aerosol Lidar (AMALi) system was installed aboard the *Polar 5* and was used to de-

Table 1. List of atmospheric variables observed and computed in this study, including meteorology, aerosol particles (APs), black carbon (BC) particles, and cloud particles.

Variable	Symbol	Unit	Instrument	Inlet	Aircraft	Size range (diameter)
Meteorology						
Temperature	T	°C	–	–	P6	–
Potential temperature	T_P	K	–	–	P6	–
Relative humidity	RH	%	–	–	P6	–
Aerosol particles						
AP number concentration	N_{AP}	cm^{-3}	UHSAS	Total	P6	80–1000 nm
AP residual number concentration	N_{AP-res}	cm^{-3}	UHSAS	CVI	P6	80–1000 nm
Black carbon particles						
BC mass concentration	M_{BC}	ng m^{-3}	SP2	Total	P6	73–575 nm
BC number concentration	N_{BC}	cm^{-3}	SP2	Total	P6	73–575 nm
BC mass-equivalent diameter	D_{BC}	nm	SP2	Total and CVI	P6	73–575 nm
BC geometric mean diameter	D_{BC-Geo}	nm	SP2	Total and CVI	P6	73–575 nm
BC modal diameter	D_{BC-Mod}	nm	SP2	Total and CVI	P6	73–575 nm
BC residual mass concentration	M_{BC-res}	ng m^{-3}	SP2	CVI	P6	73–575 nm
BC residual number concentration	N_{BC-res}	cm^{-3}	SP2	CVI	P6	73–575 nm
Cloud particles						
Droplet number concentration	N_{Dro}	cm^{-3}	SID-3	–	P6	5–45 µm
Droplet number concentration, $D > 10$ µm	N_{Dro10}	cm^{-3}	SID-3	–	P6	10–45 µm
Liquid water content	LWC	g m^{-3}	SID-3	–	P6	5–45 µm
Ice water content	IWC	g m^{-3}	CIP	–	P6	75–1550 µm
Ice water fraction	IWF	–	CIP – SID-3	–	P6	5–1550 µm
Cloud-top height	–	m a.s.l.	AMALi	–	P5	–

The abbreviations/acronyms used in the Instrument, Inlet, and Aircraft columns are as follows: UHSAS – ultra-high-sensitivity aerosol spectrometer, SP2 – single-particle soot photometer, SID-3 – Small Ice Detector Mark 3, CVI – counterflow virtual impactor, CIP – cloud imaging probe, AMALi – Airborne Mobile Aerosol Lidar, P5 – *Polar 5*, and P6 – *Polar 6*.

rive the cloud-top height. Previous works provide technical details on the operation principle (Stachlewska, 2005), data processing (Stachlewska et al., 2010), and Arctic deployment (Nakoudi et al., 2020). Cloud-top height data with a 10 s time resolution are available on PANGAEA (https://doi.org/10.1594/PANGAEA.899962; Neuber et al., 2019). We will solely discuss the cloud-top height data acquired during co-located flights of *Polar 5* and *Polar 6* that occurred on 27–29 June 2017 and 2, 5, 8, 13, and 17 June 2017, respectively.

2.2.3 Aerosol particle measurements

All aerosol particle data presented in this work were acquired with online single-particle instruments aboard *Polar 6*. A single-particle soot photometer (SP2, version D with eight channels; DMT, Longmont, CO, USA) was used to detect BC aerosol particles. While the operating principles of the SP2 and the assumptions used in this study are described briefly in the following, a comprehensive description of calibration standards and procedure has been given by Schwarz et al. (2006), Moteki and Kondo (2010), Gysel

et al. (2011), and Laborde et al. (2012). Using laser-induced incandescence, the SP2 is capable of quantifying the mass of absorbing and refractory material contained in aerosol particles passing through a high-intensity continuous-wave, intracavity laser beam at a wavelength of 1064 nm (Stephens et al., 2003). The incandescent light detector was calibrated with a fullerene soot standard from Alfa Aesar (stock no. 40971, lot no. FS12S011), size selected with a differential mobility analyser (DMA; TSI, Shoreview, MN, USA). The term "refractory black carbon" (rBC) is used to identify the insoluble carbonaceous matter that vaporizes at temperatures of around 4000 K and that is measured with a laser-induced incandescence technique, including the SP2 (Petzold et al., 2013). To facilitate the reading of this paper, the term BC is used instead of rBC to identify all measurements performed with the SP2 and presented hereafter. The SP2 installed aboard *Polar 6* provided the number concentration (N_{BC}), the mass concentration (M_{BC}), and the size distribution of BC particles in the 0.37–178 fg mass range, converted to a mass-equivalent diameter (D_{BC}) range of 73–575 nm using a fixed bulk density (void-free) of 1800 kg m^{-3} (Moteki
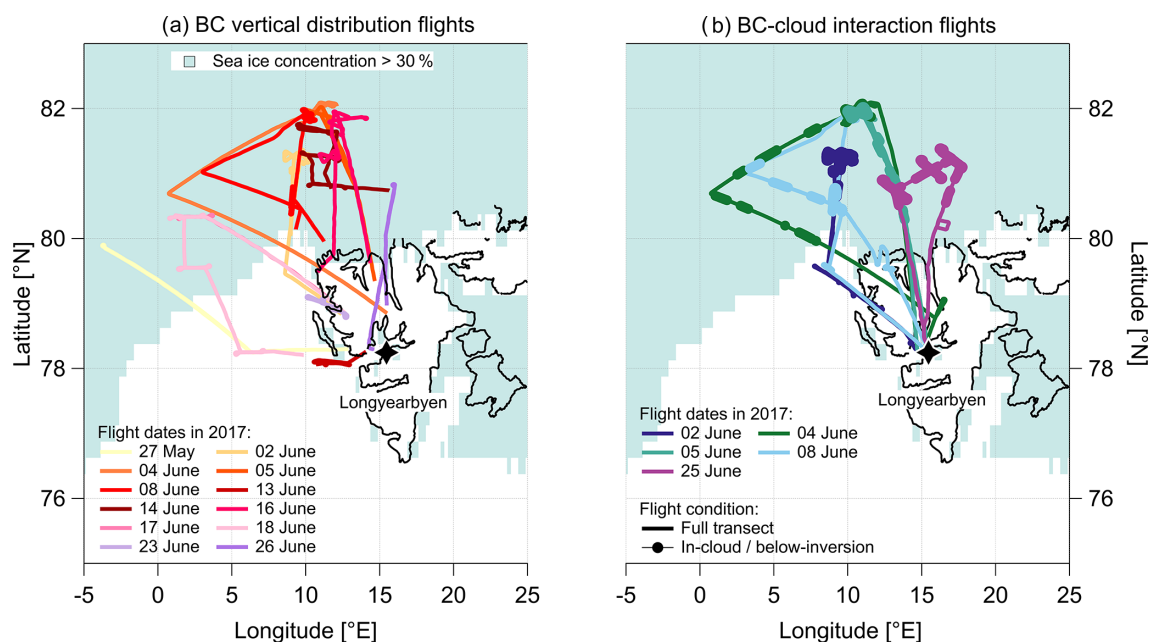
Figure 1. Map of Svalbard overlaid with the flight patterns of the *Polar 6* aircraft in May–June 2017 for the flights dedicated to investigating the vertical distribution **(a)** and cloud interaction **(b)** of BC particles. Sea ice concentration was derived from the Group for High Resolution Sea Surface Temperature (GHRSST) Level 4 Multiscale Ultrahigh Resolution (MUR) analysis product with a 0.25° resolution (MUR-JPL-L4-GLOB-v4.1; https://doi.org/10.5067/GHM25-4FJ42, Chin et al., 2017).

et al., 2010). The BC particles associated with a saturated incandesce signal were included in the last diameter bin of the size distribution and attributed to the maximum quantifiable mass-equivalent diameter (575 nm) and mass (178 fg). The geometric mean diameter and modal diameter of the mass size distribution will be abbreviated as $D_{\mathrm{BC\text{-}Geo}}$ and $D_{\mathrm{BC\text{-}Mod}}$, respectively.

To estimate the BC mass concentration outside of the SP2's detection range, the BC mass size distribution measured by the SP2 may be fitted with a lognormal fit (e.g. Laborde et al., 2013; Zanatta et al., 2018). This correction was not applied to the ACLOUD data, as a clear peak in the number size distribution was rarely resolved and the mass size distribution often culminated at the SP2's upper quantification limit. Previous studies have shown that the SP2 is sensitive to metal-containing particles such as hematite and magnetite (Schwarz et al., 2006; Yoshida et al., 2016). Hence, metal-containing dust particles may be misinterpreted as BC, causing a potential overestimation of the BC concentration. Compared with BC, hematite and magnetite are characterized by a lower boiling point and colour ratio (the ratio of thermal emission in the blue and red spectrum) as well as by a slower heating rate in the laser beam of the SP2. Hence, the temporal evolution of the incandescence signal in the laser beam of the SP2 and the colour ratio were used to identify non-BC metal-containing dust particles. During ACLOUD, particles associated with a slow rise-time of the incandesce signal from the baseline to the peak were re-

moved, and the colour ratio analysis did not show any clear evidence of the presence of non-BC incandescent particles. The optical diameter of BC-free particles was inferred with Mie theory (Bohren and Huffman, 1998) from the scattering signal acquired by avalanche photodetectors in the given solid angles under the assumption of spherical particles and a refractive index of $1.50 + 0i$. The measurement of the particle scattering cross-section was calibrated using monodisperse spherical polystyrene latex (Thermo Fisher Scientific, Waltham, Massachusetts, USA). The leading-edge-only (LEO) technique was applied to estimate the coating thickness of BC-containing particles from the optical diameter of unperturbed BC cores and BC-containing particles (Gao et al., 2007). The refractive index of the coating was assumed to be equal to BC-free particles ($1.50 + 0i$), while the refractive index of BC cores was set to $1.90 + 0.8i$. The latter, although lower than previous Arctic studies ($2.26 + 1.26i$; Raatikainen et al., 2015; Kodros et al., 2018; Zanatta et al., 2018) and higher than measurements in continental Europe ($1.75 + 0.43i$; Yuan et al., 2021), allowed one to match the mass-equivalent diameter of BC with its optical diameter. The coating thickness was quantified for BC-containing particles with a D_{BC} of between 200 and 250 nm. It must be noted that the scattering detector failed on 3 June 2017; hence, no LEO-fit analysis was performed on the following flights. BC data acquired with the SP2 are publicly available at https://doi.org/10.1594/PANGAEA.899937 (Zanatta and Herber, 2019b).

The ultra-high-sensitivity aerosol spectrometer (UHSAS; DMT, Longmont, CO, USA) measures the number concentration (N_{AP}) and size distribution of aerosol particles in the optical diameters range of 60–1000 nm (Cai et al., 2008). The UHSAS was connected in parallel to the SP2 at a tubing length distance of 15 cm. Due to the low signal-to-noise ratio at small sizes, the concentration and size distribution estimated from the UHSAS during ACLOUD were valid within the optical diameter range of 80–1000 nm (Zanatta et al., 2020). It must be noted that rapid changes in pressure might affect the sample flow measurement and, consequently, the quantification of the aerosol particle number concentration by the UHSAS (Brock et al., 2011). Although modification of the UHSAS flow system is recommended for airborne operation (Kupc et al., 2018), Schulz et al. (2019) showed no measuring bias for an unmodified UHSAS installed in the unpressurized cabin of *Polar 6* during low-speed flights. Aerosol particle data acquired with the UHSAS are publicly available at https://doi.org/10.1594/PANGAEA.900341 (Zanatta and Herber, 2019a).

2.3 Cloud and aerosol particle sampling

Two different inlets were installed on top of the *Polar 6*, at the front of the aircraft and ahead of the engines, to sample the total aerosol and cloud particle residuals. A comprehensive description of the two inlets is given by Ehrlich et al. (2019).

The total aerosol inlet was a stainless-steel inlet with a shrouded diffuser that had already been installed on the *Polar 6* during previous Arctic campaigns (Leaitch et al., 2016; Schulz et al., 2019). The manifold exhaust flowed freely into the back of the cabin, such that the intake flow varied with the true airspeed of the aircraft. Sampling speed at the inlet tip was approximately isokinetic for the airspeeds during ACLOUD, leading to a near-unity transmission of submicrometric aerosol particles (Ehrlich et al., 2019).

A counterflow virtual impactor (CVI; Ogren et al., 1985; Noone et al., 1988) allowed size-selective sampling of cloud particles by use of a counterflow at the inlet tip. Depending on the velocity of the particles inside the inlet and the flow rate of the counterflow, smaller cloud and aerosol particles may be decelerated, stopped, and blown out of the inlet. Due to the rather low velocity of the *Polar 6*, only cloud particles larger 10 µm could be sampled inside clouds by the CVI, while interstitial aerosol and gases and smaller droplets were pre-segregated. Cloud residual particles were then released following evaporation or sublimation of liquid droplets or ice crystals, respectively. Hence, cloud particle residuals were representative of cloud condensation nuclei and/or ice-nucleating particles (Mertes et al., 2005, 2007). In order to calculate the concentration of cloud particle residuals, the enrichment factor (EF) needed to be considered. The EF was calculated as the ratio between the air volume flows in front and within the CVI, which varied between a minimum of 3.2 and maximum of 5.4 with a median value of

4.2. The transmission efficiency (TE) within the CVI inlet was calculated, similar to Schroder et al. (2015), as the ratio of the number concentration of droplets larger than the CVI size cut-off (10 µm; N_{Dro-10}) measured by the SID-3 over the number concentration of aerosol particles measured by the UHSAS in the optical diameter range of 80–1000 nm and corrected by the enrichment factor of the CVI inlet. Overall, the TE varied between a flight average minimum of 16 % (5 June) and a maximum of 23 % (on 8 June), with an overall median value of 21 %. Finally, the number concentration of BC in cloud particle residuals (N_{BC-res}) was calculated as follows:

$$N_{BC\text{-}res} = \frac{N_{BC}}{EF \times TE}. \tag{1}$$

The SP2 and the UHSAS were operated in parallel and shared a sampling line which was alternatively connected to the total inlet or the CVI inlet. Outside clouds ($N_{Dro} = 0\,\mathrm{cm}^{-3}$ and LWC $= 0\,\mathrm{g\,m}^{-3}$), SP2 and UHSAS measurements were performed at the total inlet. Inside cloud ($N_{Dro} \geq 1\,\mathrm{cm}^{-3}$ and LWC $\geq 0.01\,\mathrm{g\,m}^{-3}$), the SP2 and UHSAS were sampling throughout the CVI inlet line.

3 Results

3.1 Overview of the vertical distribution of BC particles during ACLOUD

A total of 12 ACLOUD flights were selected to investigate the vertical profile of BC and cloud particles over the marginal sea ice zone, open water, and land in the northwest of Svalbard (Fig. 1a). These measurements covered the three synoptic conditions identified during the ACLOUD campaign (Knudsen et al., 2018). One flight (27 May 2017) was performed during the "cold period", when cold and dry conditions were dominant; four flights (2, 4, 5, and 8 June 2017) were performed during the "warm period" in the presence of moist air; and seven flights (13, 14, 16, 17, 18, 23, and 26 June 2017) were affected by a mixture of air masses, referred to as the "normal period".

The vertical variability in the M_{BC} and mass size distribution is shown in Fig. 2a and b, respectively. For this specific analysis, the in-cloud measurement periods were excluded. Overall, the median M_{BC} was 2.3 ng m^{-3} with an interquartile range (IQR) of 0.86–4.8 ng m^{-3}. This low concentration is expected during summer across the full Arctic (Schwarz et al., 2013; Roiger et al., 2015; Schulz et al., 2019) and is connected to the limited south–north circulation of air masses (Bozem et al., 2019) and efficient wet removal south of the polar dome (Croft et al., 2016). Although the impact of pollution plumes is not infrequent in the free troposphere in the summer Arctic (Roiger et al., 2015), the average vertical profile of M_{BC} did not show any relevant pollution plume above 500 m a.s.l., where the M_{BC} median concentration varied between 1.7 and 3.9 ng m^{-3}. On the contrary, the M_{BC} showed
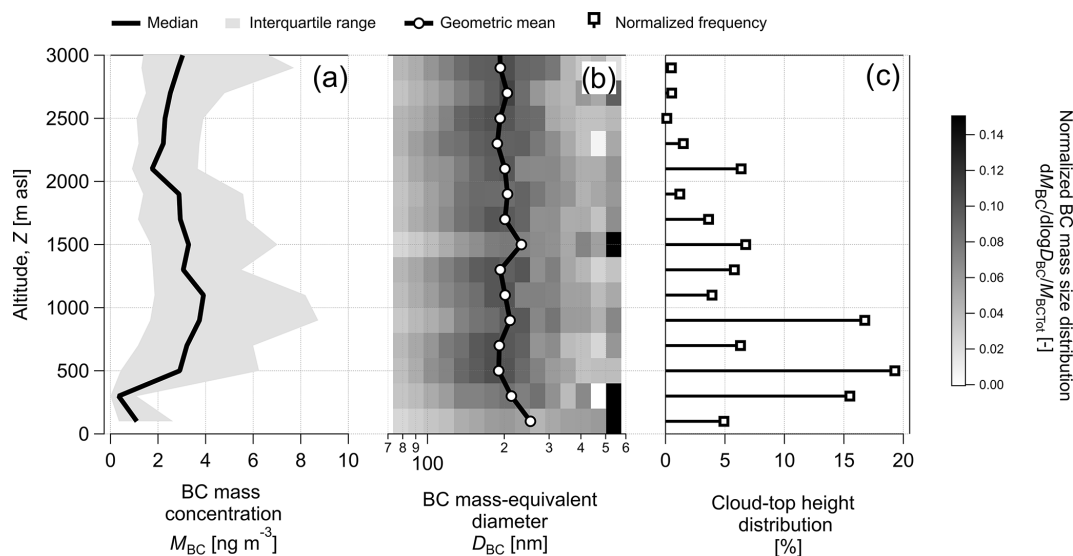
Figure 2. Vertical variability in the (**a**) BC mass concentration, (**b**) BC mass size distribution, and (**c**) cloud-top height. BC particles were sampled via the total inlet and measured with the SP2 in the 73–575 nm diameter range. Cloud top was derived from the AMALi instrument. Statistics were calculated for equidistant, 100 m thick altitude steps starting at the surface (0 m a.s.l.).

a marked decrease to less than $1\,\mathrm{ng\,m^{-3}}$ at altitudes below 500 m a.s.l. Similar to the mass concentration, the mass size distribution remained relatively stable above 500 m a.s.l. (geometric mean of the mass size distribution between 180 nm and 190) but showed an increasing concentration of larger BC particles in the lowermost atmospheric layers, where the geometric mean of the mass size distribution was 220–250 nm. While the diameter of BC particles was reported to slightly decrease with altitude in summer in various Arctic regions (Jurányi et al., 2023), the presence of large BC particles in the lowest atmospheric layer is unusual for summer conditions (Arctic Ocean; Taketani et al., 2016). These larger particles (mass geometric mean diameter above 400 nm) accounted for less than 5 % of the total number concentration along the full altitude range. Nonetheless, they represented 37 % of the total BC mass observed in the lowest 500 m a.s.l. and 17 % in atmospheric layers aloft. No evident change in mass concentration and size distribution was observed between the cold, warm, and normal periods.

During ACLOUD, cloud cover exceeded 70 %, with a preponderant occurrence of low-level clouds (Wendisch et al., 2018). AMALi lidar measurements, performed aboard the *Polar 5* during co-located flights, confirmed the presence of low-level clouds. The resulting vertical distribution of the frequency of cloud-top height (Fig. 2c) showed that 40 % of the total clouds were observed below 500 m a.s.l. Due to the variation in the BC properties in concurrence with the cloud presence in the lowest 500 m of altitude, we investigate the relationship between BC properties and low-level clouds in the following in order to understand the interaction of BC particles with clouds in the summer Arctic boundary layer.

3.2 Identification and characterization of low-level clouds

Within the warm period of the ACLOUD campaign, four consecutive flights (2, 4, 5, and 8 June 2017), conducted northwest of Svalbard between approximately 80 and 82° N (Fig. 1b), allowed for the investigation of the variability in BC particles above cloud and below cloud as well as the properties of BC residuals inside clouds. A full description of the atmospheric structure, vertical variability in the water content, and vertical coverage of aerosol particle measurements is given in the Supplement and shown in Fig. S1. The vertical profile of the potential temperature (Fig. S1a) indicated that clouds were coupled with the surface (Gierens et al., 2020) and protruded into the inversion layer but not above the inversion top; hence, they were classified as "cloud inside inversion" (Sedlar et al., 2011). In the relatively warm and moist boundary layer ($T > -6.5\,°\mathrm{C}$ and RH > 80 %; Fig. S1b), liquid droplets dominated the cloud water content (Fig. S1c), while the ice phase was observed throughout the cloud and precipitation was detected below the cloud (Fig. S1d). The cloud events discussed here showed many features common to Arctic persistent, mixed-phase clouds, as summarized by Sedlar et al. (2011), Morrison et al. (2012), and Korolev et al. (2017): the dominance of supercooled droplets, intruding-inversion clouds but coupled with the surface, and ice sedimentation below cloud. Thus, we can conclude that the selected ACLOUD cloud cases fairly represented summer Arctic conditions. Valid cloud residual measurements were performed from 60 m to 544 m a.s.l. (cloud thickness of 310–435 m). Above-cloud observations performed above the inversion top (400–750 m a.s.l.) rep-
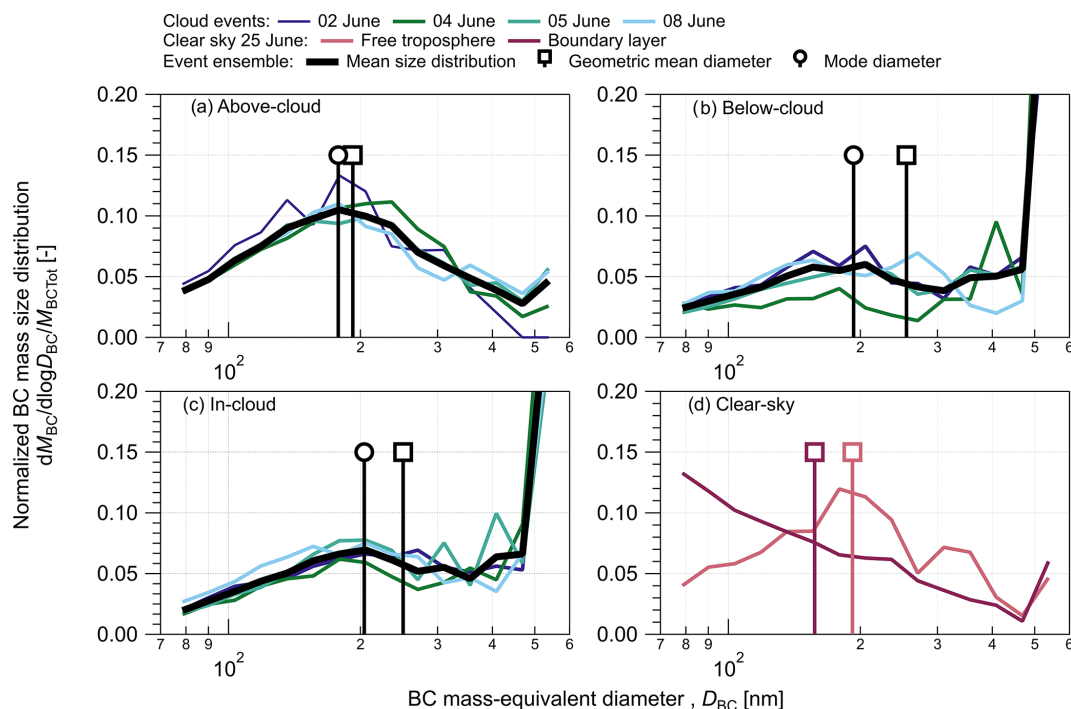
Figure 3. BC normalized mass size distribution observed **(a)** above cloud, **(b)** below cloud, **(c)** in cloud, and **(d)** under clear-sky conditions. BC residuals were sampled via the CVI inlet, while BC particles were sampled via the total inlet. Both BC residuals and BC particles were measured with the SP2 in the 73–575 nm diameter range.

resented free-tropospheric conditions, whereas below-cloud observations (60–150 m a.s.l.) represented the Arctic boundary layer influenced by cloud presence (Fig. S1e). The measurement times above, inside, and below clouds were 82, 199, and 84 min, respectively. Dominant clear-sky conditions were observed on 25 June 2017 (ACLOUD normal period) over sea ice north of Svalbard (Fig. 1b), where neither cloud droplets nor ice crystals were observed above or below inversion.

3.3 BC properties in a cloud-dominated boundary layer

To understand if cloud presence might affect the properties of BC particles in the boundary layer, we will present the variability in the concentration and size distribution of BC particles from above cloud to below cloud for the cloud events observed between 2 and 8 June 2017 as well as from above inversion to below inversion for the clear-sky event on 25 June 2017.

The flight ensemble median BC mass concentration decreased by a factor of 4 from above cloud (median $M_{BC} = 5.5$ ng m^{-3}) to below cloud (median $M_{BC} = 1.3$ ng m^{-3}) for the flights that occurred between 2 and 8 June, in agreement with the overall vertical profile shown Fig. 2a.

For all of the considered events, the mass size distribution of BC above cloud remained almost constant, with an overall geometric mean diameter (D_{BC-Geo}) of 192 nm and

a modal diameter (D_{BC-Mod}) of 178 nm. Similar values were observed in the free troposphere under clear-sky conditions on 25 June ($D_{BC-Mod} = 183$, $D_{BC-Geo} = 190$ nm; Fig. 3d). The steady state of the BC size distribution from 2 to 25 June indicated the presence of a homogeneous BC population in the free troposphere, which appeared to be independent of cloud presence below the inversion top. The mass size distribution of BC aerosol below cloud, characterized by a D_{BC-Mod} of 193 nm and a D_{BC-Geo} of 255 nm, was enriched in larger BC particles otherwise not observed in the free troposphere (Fig. 3b). In fact, BC particles larger than the saturation diameter (575 nm) represented less than 5 % of M_{BC} above cloud and 36 % of M_{BC} below cloud. In contrast, the BC mass size distribution observed under clear-sky conditions (25 June) within the boundary was depleted in particles larger than 150–200 nm and did not show any mode in the SP2 size detection range (Fig. 3d). The size distribution of free-tropospheric BC observed during ACLOUD is not uncommon in the Arctic spring and summer (Raatikainen et al., 2015; Taketani et al., 2016; Kodros et al., 2018; Zanatta et al., 2018; Schulz et al., 2019; Ohata et al., 2021). However, none of these previous Arctic studies reported BC size distributions similar to below-cloud conditions. The results presented in this section confirmed the vertical variability in the BC concentration and size presented in Sect. 3.1, clearly showing that ground observations did not represent the free troposphere. Moreover, the recurring enhancement of larger

BC particles observed below cloud compared with above cloud and its depletion in a clear-sky boundary layer suggested the influence of cloud processing on BC properties.

3.4 BC scavenging processes

The number concentration of BC residuals was low, with a median $N_{BC\text{-res}}$ of 0.58 cm^{-3} and an IQR of 0.29–1.0 cm^{-3}. The $N_{BC\text{-res}}/N_{Dro10}$ ratio ranged from a maximum median of 1.5 % on 2 June to a minimum median of 0.69 % on 4 June, with a cloud ensemble median of 0.90 % and an IQR of 0.46 %–1.4 % (Fig. 4a). The low $N_{BC\text{-res}}/N_{Dro10}$ values indicated that BC was activated in a small fraction of droplets and represented the minority of cloud-active aerosol particles. Considering that the number size distribution culminated at the low quantification limit of the SP2, $N_{BC\text{-res}}$ and $N_{BC\text{-res}}/N_{Dro10}$ were, most certainly, underestimated. To assess the activation mechanism of BC particles, we compared the absolute and relative concentration of BC residuals with BC particles sampled outside clouds.

3.4.1 Below-cloud nucleation scavenging

Earle et al. (2011) and McFarquhar et al. (2011) found that the totality of below-cloud aerosol particles was activated in cloud in the Alaskan Arctic. Following their approach, we calculated the ratio between $N_{BC\text{-res}}$ over N_{BC} measured below cloud ($N_{BC\text{-blw}}$) and above cloud ($N_{BC\text{-abv}}$). $N_{BC\text{-res}}/N_{BC\text{-abv}}$ varied from the highest median value of 0.44 on 2 June to the lowest median value of 0.25 on 8 June, with a cloud ensemble median of 0.30 (IQR = 0.18–0.47; Fig. 4b). The $N_{BC\text{-res}}/N_{BC\text{-blw}}$ median values were surprisingly high, ranging from a minimum of 1.05 on 2 June to a maximum of 1.33 on 4 June, with a cloud ensemble median of 1.16 and an IQR of 0.71–1.76 (Fig. 4c). The above-unity values of $N_{BC\text{-res}}/N_{BC\text{-blw}}$ suggested that the totality of BC particles below cloud could be activated in cloud via adiabatic lifting (Earle et al., 2011; McFarquhar et al., 2011). However, measurement uncertainty might contribute to the $N_{BC\text{-res}}/N_{BC\text{-blw}}$ values above unity. The uncertainty of $N_{BC\text{-res}}$ had two main contributions: the 1σ reproducibility of N_{BC} measured by SP2 (5 %; Laborde et al., 2012) and the uncertainty associated with the transmission efficiency factor (13 %). The latter was estimated by propagating the 1σ reproducibility associated with N_{AP} measured by the UHSAS (9 %; Ehrlich et al., 2019) and the uncertainty of N_{Dro} measured by the SID-3 (10 %; Baumgardner et al., 2017). Thus, the overall uncertainty of $N_{BC\text{-res}}/N_{BC\text{-blw}}$ (±15 %) might contribute to the $N_{BC\text{-res}}/N_{BC\text{-blw}}$ up to 1.15. Moreover, the sedimentation of ice crystals observed below cloud (Fig. S1d) might reduce $N_{BC\text{-blw}}$ by impaction scavenging (Hegg et al., 2011; Gogoi et al., 2018), thereby contributing to the enhanced $N_{BC\text{-res}}/N_{BC\text{-blw}}$ values.

3.4.2 Interstitial and above-cloud scavenging

Other activation mechanisms might contribute to the $N_{BC\text{-res}}/N_{BC\text{-blw}}$ values above unity. First, interstitial aerosol particles may be scavenged via impaction with existing droplets (Croft et al., 2016), increasing the number concentration of BC residuals (Baumgardner et al., 2008). Thus, we compared the fraction of BC particles measured outside clouds ($F_{BC} = N_{BC}/N_{AP}$) and inside clouds ($F_{BC\text{-res}} = N_{BC\text{-res}}/N_{AP\text{-res}}$). An increase in $F_{BC\text{-res}}$ compared with F_{BC} indicates interstitial impaction as the preponderant scavenging mechanism of BC particles (Baumgardner et al., 2008). During the ACLOUD cases, we found slightly smaller $F_{BC\text{-res}}$ (1.0 %) than F_{BC} above cloud (2.3 %) and below cloud (1.2 %). Similar $F_{BC\text{-res}}$ and F_{BC} below cloud suggested that BC was activated via the same pathway as the bulk aerosol, that BC and other aerosol particles shared similar hygroscopicity, and that BC particles were not preferentially entering the cloud phase by interstitial scavenging. Second, Igel et al. (2017) showed that free-tropospheric aerosol may be scavenged at the top of stratocumulus Arctic clouds protruding through the inversion layer. Considering that the clouds observed between 2 and 8 June extended into the inversion layer (Figs. S1a, 6a), the high N_{BC} observed above cloud represented a non-negligible source of hygroscopic BC particles which might have contributed to the $N_{BC\text{-res}}/N_{BC\text{-blw}}$ values above unity reported above. To better understand the contribution of below-cloud and above-cloud activation processes, we further analysed the size distribution and mixing state of BC residuals in Sect. 3.5 and their vertical variability in Sect. 3.6.

3.5 Characterization of BC residual properties

Diameter and mixing state are fundamental properties controlling the ability of aerosol particles to nucleate a liquid droplet (hygroscopicity). Previous studies have shown that larger and internally mixed BC are more hygroscopic (Dalirian et al., 2018; Motos et al., 2019a) and are enriched in the residual phase compared with outside clouds (Motos et al., 2019b). Hence, to assess the nucleation scavenging during ACLOUD, we present the coating thickness and size distribution of BC residuals and their variation compared with conditions outside of the cloud.

3.5.1 Coating thickness of BC residuals on 2 June

Due to failure of the scattering detector, the quantification of coating thickness was only possible for the flight that occurred on 2 June. Considering that the coating thickness was quantified for BC cores in the 200–250 nm diameter range, which represented a small subset of the total detected BC particles, the results discussed here are extremely uncertain due to the low counting statistics. However, BC cores in the 200–250 nm diameter range were ubiquitously found above cloud, inside cloud, and below cloud (Fig. 3). The distribution of
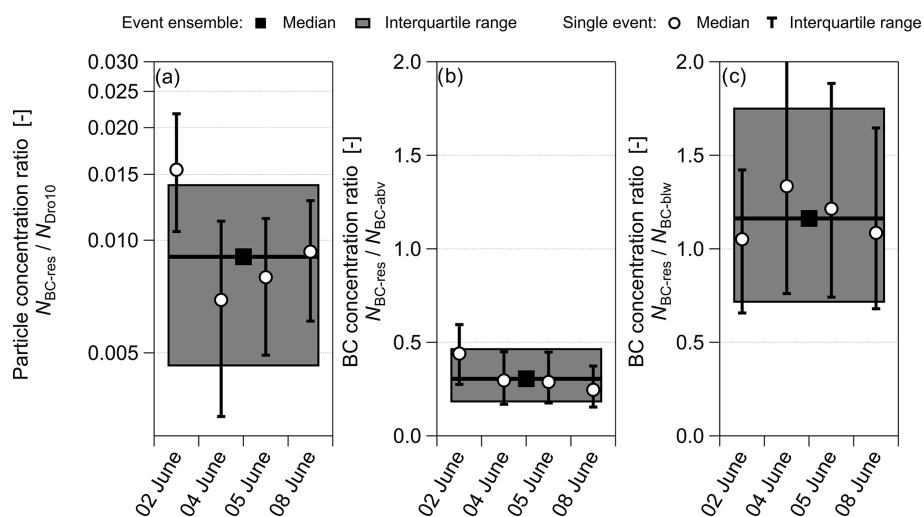
Figure 4. Box plots of the BC concentration in cloud residuals showing **(a)** the ratio between the number concentration of cloud residuals (N_{BC-res}) and the liquid droplet number concentration (N_{Dro10}), **(b)** the ratio between the number concentration of cloud residuals (N_{BC-res}) and the number concentration of BC particles measured above cloud (N_{BC-abv}), and **(c)** the ratio between the number concentration of cloud residuals (N_{BC-res}) and the number concentration of BC particles measured below cloud (N_{BC-blw}). Liquid droplets were measured with the SID-3 probe in the 10–45 µm diameter range. BC residuals were sampled via the CVI inlet, while BC particles were sampled via the total inlet. Both BC residuals and BC particles were measured with the SP2 in the 73–575 nm diameter range.

coating thickness is presented in Fig. S2. The thinnest coatings were observed above clouds, where the coating thickness median was 30 nm (IQR = 23–48 nm) and the median shell-to-core ratio was 1.51 (IQR = 1.38–1.8). The thickest coatings were observed below clouds, where the median coating thickness was 43 nm (IQR = 25–58 nm) and the median shell-to-core diameter ratio was 1.67 (IQR = 1.43–1.98). The BC cloud residuals showed a medium coating thickness (median of 38 nm, IQR of 25–59 nm) and shell-to-core ratio (median of 1.58, IQR of 1.39–1.92 nm) compared with above and below cloud. The coating thickness values presented here are similar to previous Arctic ground (Raatikainen et al., 2015; Zanatta et al., 2018) and airborne (Kodros et al., 2018; Ohata et al., 2021) observations and are substantially higher than urban observations (Laborde et al., 2013; Yoshida et al., 2020). Even though thicker coatings can be found in aged continental air masses, the presence of 30–40 nm thick coatings is sufficient to significantly increase the hygroscopicity of otherwise hydrophobic uncoated BC particles in laboratory experiments (Dalirian et al., 2018) and field observations (Motos et al., 2019a). Keeping in mind the low counting statistics of the coating analysis, we can conclude that BC particles sampled during ACLOUD represented aged and hygroscopic BC particles, which could be efficiently activated via nucleation scavenging. However, the reduced temporal coverage and the uncertainty of coating thickness quantification (17 %; Laborde et al., 2012) did not allow for the identification of a significant change in the degree of internal mixing between BC residuals and BC particles sampled outside clouds.

3.5.2 Size distribution of BC residuals

The mass size distribution of BC residuals was similar during all cloud cases (Fig. 3c), indicating similar conditions along the measuring period. While an evident mode at 193 nm was comparable to BC particles observed above and below cloud, the size distribution of BC residuals showed a prominent shoulder towards larger diameters, culminating in the overflow saturation bin (BC cores larger than 575 nm of mass-equivalent diameter, representing 28 % of the M_{BC-res}). This feature was shared only with BC particles sampled below cloud. The almost bimodal distribution observed inside cloud and below cloud suggested the occurrence of different cloud processes. On the one hand, the recurring peak around 180–200 nm in the BC size distribution outside and inside cloud reinforced the hypothesis of cloud-mediated transport of free-tropospheric BC in the boundary layer proposed by Igel et al. (2017). On the other hand, the similar size distributions of BC residuals and BC particles sampled below cloud clearly indicated an efficient exchange of BC particles at the cloud bottom. This exchange might include nucleation from the below-cloud layer (Earle et al., 2011; McFarquhar et al., 2011) followed by the release of BC residuals contained in precipitating droplets below cloud (Igel et al., 2017). As suggested for ice-nucleating particles in persistent low-level Arctic clouds by Solomon et al. (2015), this activation and release cycle might occur several times.

To quantify the size-dependent enrichment or depletion of BC in cloud residuals compared with outside cloud, we calculated the ratio of the number size distribution of BC residuals over the number size distribution of BC particles sam-
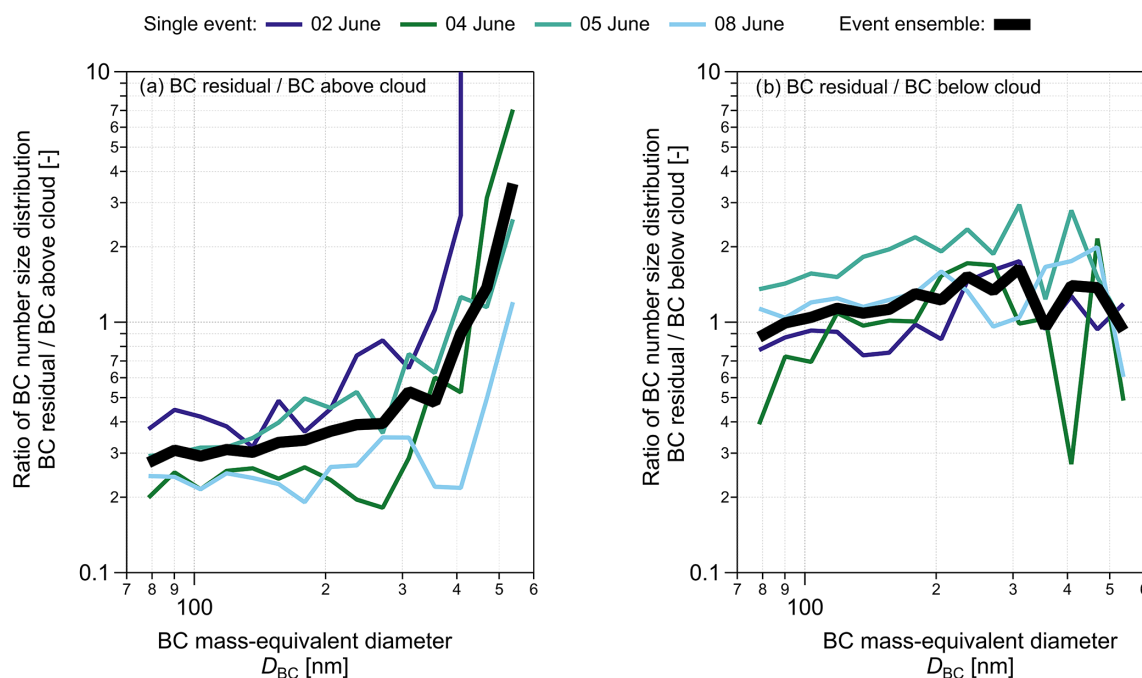
Figure 5. Ratio of the number size distribution of BC residuals over the number size distribution of BC particles sampled above cloud **(a)** and below cloud **(b)**. BC residuals were sampled via the CVI inlet, while BC particles were sampled via the total inlet. Both BC residuals and BC particles were measured with the SP2 in the 73–575 nm diameter range.

pled above cloud and below cloud. BC residuals were depleted compared with above-cloud BC particles, especially in the 80–300 nm D_{BC} range (Fig. 5a). However, BC particles larger than 400 nm were exponentially enriched in cloud residuals (by a factor of 1.5–3.5) compared with above-cloud conditions. The ratio of the number size distribution was different for below-cloud BC (Fig. 5b), where it increased from approximately 1 for a D_{BC} below 100 nm to values of around 1.5 for a D_{BC} larger than 200 nm. First, these results confirmed that larger and more hygroscopic BC particles are usually enriched in cloud residuals (Motos et al., 2019a). Second, the values above unity shown in Fig. 5, indicating an absolute enrichment in larger BC residuals compared with above cloud and below cloud, suggested the formation of these larger BC as the result of in-cloud processing.

3.6 Vertical structure of cloud microphysics and BC residuals

In the following, we investigate the vertical variability in the cloud phase and BC residuals to understand the influence of activation from above cloud and below cloud and to identify any potential cloud processes and their potential effects on BC residual properties.

3.6.1 Normalized altitudes

Due to the low counting statistics caused by the low concentration of ice crystals and BC particles, this analysis is based exclusively on the cloud ensemble. As cloud-top and cloud-bottom height showed some variability during the different flights (Fig. S1), the vertical variability in the cloud and residual properties are presented as a function of the in-cloud normalized altitude (Z_n) following Mioche et al. (2017):

$$Z_n = \frac{Z - Z_b}{Z_t - Z_b}, \tag{2}$$

where Z is the measurement altitude, Z_b is the lowest altitude of in-cloud valid BC residual measurements, and Z_t is the highest altitude of in-cloud BC residual measurements. Thus, $Z_n = 1$ and $Z_n = 0$ correspond to the highest and lowest BC residual measurement, respectively. Considering the relatively thin clouds (vertical extent between 310 and 435 m), the cloud layer was divided into four vertical sections (quartiles).

3.6.2 In-cloud vertical profiles

The vertical profile of potential temperature indicated the presence of a homogenous and well-mixed cloud section extending from cloud bottom to $Z_n = 0.75$, where median T_{Pot} values varied by 0.25 K. Increasing T_{Pot} at $Z_n > 0.75$ indicated the cloud intrusion in the inversion layer (Fig. 6a). The LWC showed an increasing trend from cloud bottom until $Z_n = 0.75$, where the median LWC was $0.27\,g\,m^{-3}$, and a decreasing trend in the upper quartile of the cloud ensemble (Fig. 6b). The IWC increased by 2 orders of magnitude
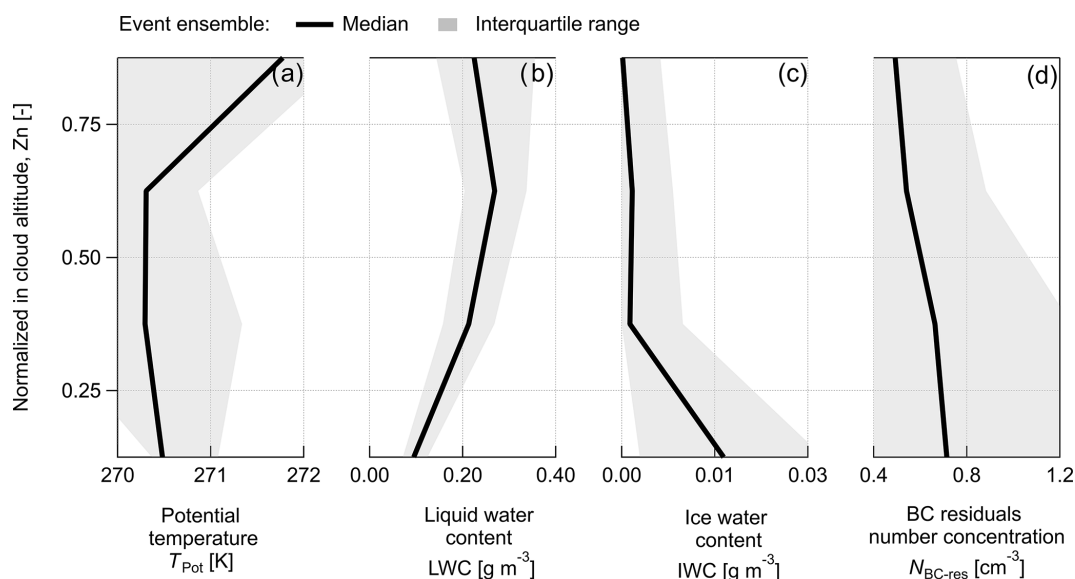
Figure 6. Vertical profiles of the cloud ensemble showing **(a)** the potential temperature (T_{Pot}), **(b)** the liquid water content (LWC), **(c)** the ice water content (IWC), and **(d)** the BC residual number concentration (N_{BC-res}). The median and interquartile range were calculated for equidistant normalized altitude (Z_n) steps of 0.25. Liquid droplets were measured with the SID-3 probe in the 5–45 µm diameter range. Ice crystals were measured with the CIP probe in the 75–1550 µm diameter range. BC residuals were sampled via the CVI inlet and measured with the SP2 in the 73–575 nm diameter range.

from 1.4×10^{-4} at cloud top to 1.8×10^{-2} g m^{-3} at cloud bottom (Fig. 6c). The number concentration of BC residuals increased monotonically from 0.50 at cloud top to 0.73 cm^{-3} at cloud bottom (Fig. 6d). The relative change in N_{BC-res} between vertically adjacent quartiles was in the uncertainty range (14 %; see Sect. 2.2.3), while a T-test analysis indicated that the hypothesis of equal N_{BC-res} averages was confirmed for the two lowermost quartiles ($Z_n < 0.50$) but not for the two uppermost quartiles ($Z_n > 0.5$). Thus, we cannot conclude that the vertical trend (quartile by quartile) in N_{BC-res} was statistically significant. However, the cloud top ($Z_n > 0.75$) and the cloud bottom ($Z_n < 0.25$) showed a statistically significant difference, not only with respect to the number concentration of BC residuals but also with respect to the potential temperature and cloud phase. Thus, we directly compare the cloud top to the cloud bottom.

3.6.3 BC residual properties in a liquid cloud top and in a mixed-phase cloud bottom

In the upper quartile of the cloud, although liquid droplets dominated the cloud phase (IWF ~ 0 %), only 0.8 % of droplets contained a BC residual, and the mass size distribution of BC residuals showed a dominant peak around 200 nm ($D_{BC-Mod} = 188$ nm; Fig. 7), similar to above-cloud BC (Fig. 3a). However, a marked tail towards larger diameters was present in the mass size distribution ($D_{BC-Geo} = 231$ nm), being more similar to below-cloud conditions (Fig. 3b). The BC residuals with a mass-equivalent diameter larger than 400 nm accounted for 36 % of the total BC mass

at the cloud top, being closer to below-cloud values (45 %) than above-cloud (11 %) values. The cloud phase and BC residual properties were different at the cloud bottom. Less and smaller liquid droplets but more and larger ice crystals (Fig. S3) led to an increase in IWF up to 14 % at the cloud bottom, where higher N_{BC-res} was observed (+31 %) compared with the cloud top, and 1.3 % of liquid droplets contained a BC residual. The mass size distribution of BC residuals at cloud bottom was almost identical to the cloud top for D_{BC} below 200 nm (Fig. 7). However, due to the increasing concentration of larger BC residuals at cloud bottom, we did not observe a clear peak in the mass size distribution (as observed at the cloud top, above cloud, and below cloud), leading to a D_{BC-Geo} of 318 nm (+38 % compared with the cloud top). Overall, BC residuals larger than 400 nm accounted for the majority of the total M_{BC-res} (62 %) at the cloud bottom.

The data presented in this section showed, for the first time, that the population of BC residuals in an Arctic cloud is not homogeneous on the vertical scale, indicating that BC might be scavenged or processed via different pathways, complicating the interpretation of our results. Considering the activation mechanisms, the higher concentration of BC residuals at the cloud bottom suggests the predominance of activation at the cloud bottom (Earle et al., 2011). However, the increase in T_{Pot} at the cloud top confirmed the intrusion of the cloud into the inversion layer (Sedlar et al., 2011) and reinforces the hypothesis of nucleation scavenging of free-tropospheric BC at the cloud top (Igel et al., 2017), which might contribute to a higher concentration of
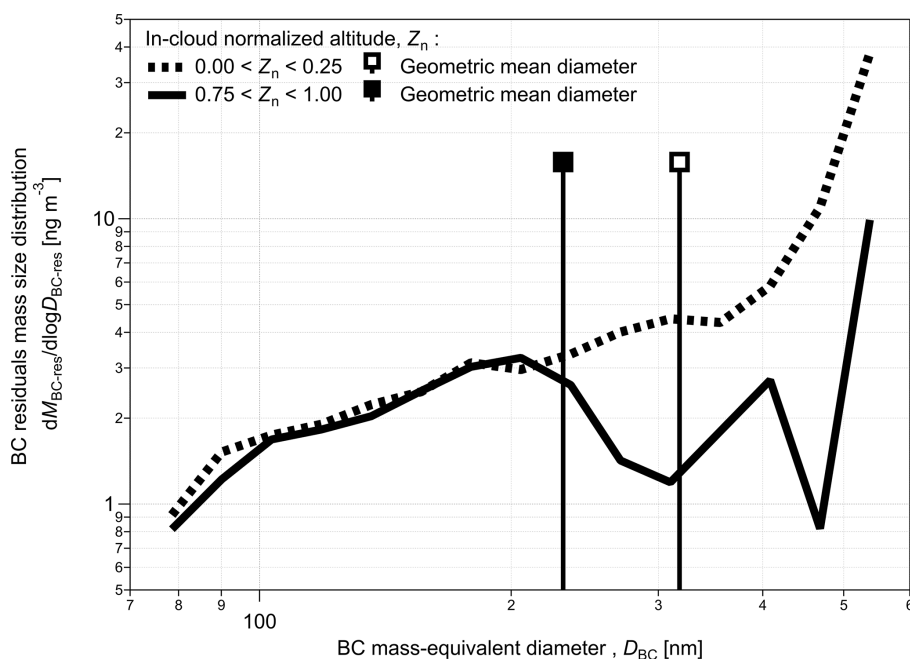
Figure 7. Mass size distribution of BC residuals measured at the cloud top ($0.75 < Z_n < 1.00$) and cloud bottom ($0.00 < Z_n > 0.25$). BC residuals were sampled via the CVI inlet and measured with the SP2 in the 73–575 nm diameter range.

$N_{BC\text{-}res}$ compared with $N_{BC\text{-}blw}$ (Fig. 4c). If the preferential nucleation scavenging of larger BC particles (Motos et al., 2019a, b) might explain the diameter increase inside the cloud compared with outside of the cloud (Fig. 5), cloud processing might also contribute to the increase in BC residuals' size within the cloud. Drizzle droplets, observed during the warm period of ACLOUD (Järvinen et al., 2023), may collect multiple droplets during sedimentation. Hence, a few large drizzle droplets may contain multiple BC residuals, which might be released as larger BC agglomerates after evaporation (Ding et al., 2019).

Due to the low transmission efficiency of large drizzle drops in the CVI inlet, we were unable to verify the correlation between the diameter of BC residuals and the concentration of drizzling drops. However, the below-cloud release via evaporation (Igel et al., 2017) of BC agglomerates formerly contained in drizzling drops and their reactivation at cloud bottom (Solomon et al., 2015) might contribute to the presence of larger BC residuals at cloud bottom (Fig. 7) and explain the similarity between the in-cloud and below-cloud size distribution (Fig. 3b, c). The increase in the IWC at cloud bottom adds an additional degree of complexity. As shown by Ding et al. (2019), different processes such as the WBF process and riming might modify the phase partitioning and size distribution of BC residuals in mixed-phase clouds. However, with our dataset, we were unable to confirm nor exclude the occurrence of liquid- and ice-driven physical modification of BC residuals.

4 Conclusions

The interaction of BC particles with Arctic clouds was investigated with airborne measurements in the northwest of Svalbard (Norway) within the framework of the ACLOUD campaign in summer 2017. The overall vertical variability in the BC properties during the ACLOUD campaign indicated a net decrease in the BC mass concentration and an increase in the BC diameter in the lowest atmospheric layer dominated by clouds. Four case events characterized by the presence of low-level, surface-coupled, inside-inversion, and mixed-phase clouds were identified.

The analysis of these events confirmed a net separation of BC properties from the atmospheric layers above cloud in the free troposphere to the below-cloud layer, where less (median BC mass concentration of $1.4\,\mathrm{ng\,m^{-3}}$), larger (geometric mean of the mass size distribution of 251 nm), and more coated (median coating thickness of 43 nm) BC particles were observed compared with above-cloud conditions (median BC mass concentration of $5.5\,\mathrm{ng\,m^{-3}}$, geometric mean of the mass size distribution of 189 nm, and median coating thickness of 30 nm). In the absence of clouds, BC particles in the boundary layer were dominated by small diameters (geometric mean of the mass size distribution of 147 nm).

Under mixed-phase cloud conditions (median temperature of $-5.3\,°C$, median LWC of $0.15\,g\,cm^{-3}$, and median IWC of $0.002\,g\,cm^{-3}$), only a small minority of droplets (less than 1 %) contained a BC particle. It appeared that the totality of BC particles below the cloud layer was activated, with potential activation of free-tropospheric BC in the cloud top extending in the inversion layer. The population of cloud residuals was enriched in larger BC particles compared with above-cloud conditions (geometric mean of the mass size distribution of 249 nm), very similar to below-cloud BC. This similarity suggested the efficient exchange of BC particles between the cloud and below-cloud layers. The vertical profiling of the cloud layer showed a clear stratification of BC residual properties from the liquid cloud-top protruding in the inversion layer to the mixed-phase cloud bottom, potentially suggesting metamorphism of BC residuals caused by cloud processing.

To conclude, the ACLOUD observations demonstrated that surface measurements are clearly not representative of the atmosphere aloft. This statement becomes particularly important in the presence of low-level, mixed-phase, persistent clouds, as recurring cloud processing in these clouds may influence not only the vertical distribution of BC but also its microphysical properties inside cloud and below cloud. Considering the short duration of our measurements and the complexity of aerosol–cloud interaction, more observations are needed to constrain activation mechanisms of BC and the impacts of cloud processing in the Arctic.

Code and data availability. The software used in this work to treat the SP2 data is available upon request from Droplet Measurement Technologies. The following ACLOUD campaign observational data are archived on the PANGAEA repository: aircraft measurements of aerosol size distribution in the Arctic during the ACLOUD campaign 2017 (https://doi.org/10.1594/PANGAEA.900341; Zanatta and Herber, 2019a); aircraft measurements of refractory black carbon in the Arctic during the ACLOUD campaign 2017 (https://doi.org/10.1594/PANGAEA.899937; Zanatta and Herber, 2019b); CDP, CIP, and PIP in situ Arctic cloud microphysical properties observed during the ACLOUD-AC3 campaign in June 2017 (https://doi.org/10.1594/PANGAEA.899074; Dupuy et al., 2019); cloud-top altitudes observed with an airborne lidar (https://doi.org/10.1594/PANGAEA.899962; Neuber et al., 2019); 1Hz resolution aircraft measurements of wind and temperature during the ACLOUD campaign in 2017 (https://doi.org/10.1594/PANGAEA.902849; Hartmann et al., 2019); and SID-3 liquid- and ice-phase particle size distributions measured during ACLOUD (https://doi.org/10.1594/PANGAEA.960269; Järvinen and Schnaiter, 2023).

Supplement. The supplement related to this article is available online at: https://doi.org/10.5194/acp-23-7955-2023-supplement.

Review statement. This paper was edited by Luis A. Ladino and reviewed by Darrel Baumgardner and two anonymous referees.

References

Baumgardner, D., Jonsson, H., Dawson, W., O'Connor, D., and Newton, R.: The cloud, aerosol and precipitation spectrometer: a new instrument for cloud investigations, Atmos. Res., 59–60, 251–264, https://doi.org/10.1016/S0169-8095(01)00119-3, 2001.

Baumgardner, D., Subramanian, R., Twohy, C., Stith, J., and Kok, G.: Scavenging of black carbon by ice crystals over the northern Pacific, Geophys. Res. Lett., 35, L22815, https://doi.org/10.1029/2008GL035764, 2008.

Baumgardner, D., Abel, S. J., Axisa, D., Cotton, R., Crosier, J., Field, P., Gurganus, C., Heymsfield, A., Korolev, A., Krämer, M., Lawson, P., McFarquhar, G., Ulanowski,

Z., and Um, J.: Cloud Ice Properties: In Situ Measurement Challenges, Meteorol. Monogr., 58, 9.1–9.23, https://doi.org/10.1175/AMSMONOGRAPHS-D-16-0011.1, 2017.

Bellouin, N., Quaas, J., Gryspeerdt, E., Kinne, S., Stier, P., Watson-Parris, D., Boucher, O., Carslaw, K. S., Christensen, M., Daniau, A.-L., Dufresne, J.-L., Feingold, G., Fiedler, S., Forster, P., Gettelman, A., Haywood, J. M., Lohmann, U., Malavelle, F., Mauritsen, T., McCoy, D. T., Myhre, G., Mülmenstädt, J., Neubauer, D., Possner, A., Rugenstein, M., Sato, Y., Schulz, M., Schwartz, S. E., Sourdeval, O., Storelvmo, T., Toll, V., Winker, D., and Stevens, B.: Bounding Global Aerosol Radiative Forcing of Climate Change, Rev. Geophys., 58, e2019RG000660, https://doi.org/10.1029/2019RG000660, 2020.

Bohren, C. F. and Huffman, D. R.: Absorption and Scattering of Light by Small Particles, Wiley-VCH Verlag GmbH, Weinheim, Germany, https://doi.org/10.1002/9783527618156.ch4, 1998.

Bond, T. C., Streets, D. G., Yarber, K. F., Nelson, S. M., Woo, J.-H., and Klimont, Z.: A technology-based global inventory of black and organic carbon emissions from combustion, J. Geophys. Res.-Atmos., 109, D14203, https://doi.org/10.1029/2003JD003697, 2004.

Bozem, H., Hoor, P., Kunkel, D., Köllner, F., Schneider, J., Herber, A., Schulz, H., Leaitch, W. R., Aliabadi, A. A., Willis, M. D., Burkart, J., and Abbatt, J. P. D.: Characterization of transport regimes and the polar dome during Arctic spring and summer using in situ aircraft measurements, Atmos. Chem. Phys., 19, 15049–15071, https://doi.org/10.5194/acp-19-15049-2019, 2019.

Brock, C. A., Cozic, J., Bahreini, R., Froyd, K. D., Middlebrook, A. M., McComiskey, A., Brioude, J., Cooper, O. R., Stohl, A., Aikin, K. C., de Gouw, J. A., Fahey, D. W., Ferrare, R. A., Gao, R.-S., Gore, W., Holloway, J. S., Hübler, G., Jefferson, A., Lack, D. A., Lance, S., Moore, R. H., Murphy, D. M., Nenes, A., Novelli, P. C., Nowak, J. B., Ogren, J. A., Peischl, J., Pierce, R. B., Pilewskie, P., Quinn, P. K., Ryerson, T. B., Schmidt, K. S., Schwarz, J. P., Sodemann, H., Spackman, J. R., Stark, H., Thomson, D. S., Thornberry, T., Veres, P., Watts, L. A., Warneke, C., and Wollny, A. G.: Characteristics, sources, and transport of aerosols measured in spring 2008 during the aerosol, radiation, and cloud processes affecting Arctic Climate (ARCPAC) Project, Atmos. Chem. Phys., 11, 2423–2453, https://doi.org/10.5194/acp-11-2423-2011, 2011.

Brown, P. R. A. and Francis, P. N.: Improved Measurements of the Ice Water Content in Cirrus Using a Total-Water Probe, J. Atmos. Ocean. Tech., 12, 410–414, https://doi.org/10.1175/1520-0426(1995)012<0410:IMOTIW>2.0.CO;2, 1995.

Cai, Y., Montague, D. C., Mooiweer-Bryan, W., and Deshler, T.: Performance characteristics of the ultra high sensitivity aerosol spectrometer for particles between 55 and 800 nm: Laboratory and field studies, J. Aerosol Sci., 39, 759–769, https://doi.org/10.1016/j.jaerosci.2008.04.007, 2008.

Chin, T. M., Vazquez-Cuervo, J., and Armstrong, E. M.: A multi-scale high-resolution analysis of global sea surface temperature, Remote Sens. Environ., 200, 154–169, https://doi.org/10.1016/j.rse.2017.07.029, 2017.

Croft, B., Martin, R. V., Leaitch, W. R., Tunved, P., Breider, T. J., D'Andrea, S. D., and Pierce, J. R.: Processes controlling the annual cycle of Arctic aerosol number and size distributions, Atmos. Chem. Phys., 16, 3665–3682, https://doi.org/10.5194/acp-16-3665-2016, 2016.

Crosier, J., Bower, K. N., Choularton, T. W., Westbrook, C. D., Connolly, P. J., Cui, Z. Q., Crawford, I. P., Capes, G. L., Coe, H., Dorsey, J. R., Williams, P. I., Illingworth, A. J., Gallagher, M. W., and Blyth, A. M.: Observations of ice multiplication in a weakly convective cell embedded in supercooled mid-level stratus, Atmos. Chem. Phys., 11, 257–273, https://doi.org/10.5194/acp-11-257-2011, 2011.

Dalirian, M., Ylisirniö, A., Buchholz, A., Schlesinger, D., Ström, J., Virtanen, A., and Riipinen, I.: Cloud droplet activation of black carbon particles coated with organic compounds of varying solubility, Atmos. Chem. Phys., 18, 12477–12489, https://doi.org/10.5194/acp-18-12477-2018, 2018.

Ding, S., Zhao, D., He, C., Huang, M., He, H., Tian, P., Liu, Q., Bi, K., Yu, C., Pitt, J., Chen, Y., Ma, X., Chen, Y., Jia, X., Kong, S., Wu, J., Hu, D., Hu, K., Ding, D., and Liu, D.: Observed Interactions Between Black Carbon and Hydrometeor During Wet Scavenging in Mixed-Phase Clouds, Geophys. Res. Lett., 46, 8453–8463, https://doi.org/10.1029/2019GL083171, 2019.

Dou, T.-F. and Xiao, C.-D.: An overview of black carbon deposition and its radiative forcing over the Arctic, Adv. Clim. Change Res., 7, 115–122, https://doi.org/10.1016/j.accre.2016.10.003, 2016.

Dupuy, R., Jourdan, O., Mioche, G., Gourbeyre, C., Leroy, D., and Schwarzenböck, A.: CDP, CIP and PIP In-situ arctic cloud microphysical properties observed during ACLOUD-AC3 campaign in June 2017, PANGAEA [data set], https://doi.org/10.1594/PANGAEA.899074, 2019.

Earle, M. E., Liu, P. S. K., Strapp, J. W., Zelenyuk, A., Imre, D., McFarquhar, G. M., Shantz, N. C., and Leaitch, W. R.: Factors influencing the microphysics and radiative properties of liquid-dominated Arctic clouds: Insight from observations of aerosol and clouds during ISDAC, J. Geophys. Res.-Atmos., 116, D00T09, https://doi.org/10.1029/2011JD015887, 2011.

Ehrlich, A., Wendisch, M., Lüpkes, C., Buschmann, M., Bozem, H., Chechin, D., Clemen, H.-C., Dupuy, R., Eppers, O., Hartmann, J., Herber, A., Jäkel, E., Järvinen, E., Jourdan, O., Kästner, U., Kliesch, L.-L., Köllner, F., Mech, M., Mertes, S., Neuber, R., Ruiz-Donoso, E., Schnaiter, M., Schneider, J., Stapf, J., and Zanatta, M.: A comprehensive in situ and remote sensing data set from the Arctic CLoud Observations Using airborne measurements during polar Day (ACLOUD) campaign, Earth Syst. Sci. Data, 11, 1853–1881, https://doi.org/10.5194/essd-11-1853-2019, 2019.

Flanner, M. G.: Arctic climate sensitivity to local black carbon, J. Geophys. Res.-Atmos, 118, 1840–1851, https://doi.org/10.1002/jgrd.50176, 2013.

Flanner, M. G., Zender, C. S., Hess, P. G., Mahowald, N. M., Painter, T. H., Ramanathan, V., and Rasch, P. J.: Springtime warming and reduced snow cover from carbonaceous particles, Atmos. Chem. Phys., 9, 2481–2497, https://doi.org/10.5194/acp-9-2481-2009, 2009.

Gao, R. S., Schwarz, J. P., Kelly, K. K., Fahey, D. W., Watts, L. A., Thompson, T. L., Spackman, J. R., Slowik, J. G., Cross, E. S., Han, J.-H., Davidovits, P., Onasch, T. B., and Worsnop, D. R.: A Novel Method for Estimating Light-Scattering Properties of Soot Aerosols Using a Modified Single-Particle Soot Photometer, Aerosol Sci. Tech., 41, 125–135, https://doi.org/10.1080/02786820601118398, 2007.

Garrett, T. J., Brattström, S., Sharma, S., Worthy, D. E. J., and Novelli, P.: The role of scavenging in the seasonal transport of black carbon and sulfate to the Arctic, Geophys. Res. Lett., 38, L16805, https://doi.org/10.1029/2011GL048221, 2011.

Gierens, R., Kneifel, S., Shupe, M. D., Ebell, K., Maturilli, M., and Löhnert, U.: Low-level mixed-phase clouds in a complex Arctic environment, Atmospheric Chem. Phys., 20, 3459–3481, https://doi.org/10.5194/acp-20-3459-2020, 2020.

Gogoi, M. M., Babu, S. S., Pandey, S. K., Nair, V. S., Vaishya, A., Girach, I. A., and Koushik, N.: Scavenging ratio of black carbon in the Arctic and the Antarctic, Polar Sci., 16, 10–22, https://doi.org/10.1016/j.polar.2018.03.002, 2018.

Gysel, M., Laborde, M., Olfert, J. S., Subramanian, R., and Gröhn, A. J.: Effective density of Aquadag and fullerene soot black carbon reference materials used for SP2 calibration, Atmos. Meas. Tech., 4, 2851–2858, https://doi.org/10.5194/amt-4-2851-2011, 2011.

Hartmann, J., Lüpkes, C., and Chechin, D.: 1Hz resolution aircraft measurements of wind and temperature during the ACLOUD campaign in 2017, PANGAEA [data set], https://doi.org/10.1594/PANGAEA.902849, 2019.

Hegg, D. A., Clarke, A. D., Doherty, S. J., and Ström4, J.: Measurements of black carbon aerosol washout ratio on Svalbard, Tellus B, 63, 891–900, https://doi.org/10.1111/j.1600-0889.2011.00577.x, 2011.

Herber, A. B., Haas, C., Stone, R. S., Bottenheim, J. W., Liu, P., Li, S.-M., Staebler, R. M., Strapp, J. W., and Dethloff, K.: Regular airborne surveys of Arctic sea ice and atmosphere, Eos Trans. Am. Geophys. Union, 93, 41–42, https://doi.org/10.1029/2012EO040001, 2012.

Hirst, E., Kaye, P. H., Greenaway, R. S., Field, P., and Johnson, D. W.: Discrimination of micrometre-sized ice and super-cooled droplets in mixed-phase cloud, Atmos. Environ., 35, 33–47, https://doi.org/10.1016/S1352-2310(00)00377-0, 2001.

Holopainen, E., Kokkola, H., Laakso, A., and Kühn, T.: In-cloud scavenging scheme for sectional aerosol modules – implementation in the framework of the Sectional Aerosol module for Large Scale Applications version 2.0 (SALSA2.0) global aerosol module, Geosci. Model Dev., 13, 6215–6235, https://doi.org/10.5194/gmd-13-6215-2020, 2020.

Igel, A. L., Ekman, A. M. L., Leck, C., Tjernström, M., Savre, J., and Sedlar, J.: The free troposphere as a potential source of arctic boundary layer aerosol particles, Geophys. Res. Lett., 44, 7053–7060, https://doi.org/10.1002/2017GL073808, 2017.

IPCC: Climate Change 2021: The Physical Science Basis, edited by: Masson-Delmotte, V., Zhai, P., Pirani, A., Connors, S. L., Péan, C., Berger, S., Caud, N., Chen, Y., Goldfarb, L., Gomis, M. I., Huang, M., Leitzell, K., Lonnoy, E., Matthews, J. B. R., Maycock, T. K., Waterfield, T., Yelekçi, O., Yu, R., and Zhou, B., Contribution of Working Group I to the Sixth Assessment Report of the Intergovernmental Panel on Climate Change, https://doi.org/10.1017/9781009157896, 2021.

Järvinen, E. and Schnaiter, M.: SID-3 Liquid and Ice Phase Particle Size Distributions measured during ACLOUD, PANGAEA [data set], https://doi.org/10.1594/PANGAEA.960269, 2023.

Järvinen, E., Nehlert, F., Xu, G., Waitz, F., Mioche, G., Dupuy, R., Jourdan, O., and Schnaiter, M.: Investigating the vertical extent and short-wave radiative effects of the ice phase in Arctic sum-

mertime low-level clouds, Atmos. Chem. Phys., 23, 7611–7633, https://doi.org/10.5194/acp-23-7611-2023, 2023.

Jurányi, Z., Zanatta, M., Lund, M. T., Samset, B. H., Skeie, R. B., Sharma, S., Wendisch, M., and Herber, A.: Atmospheric concentrations of black carbon are substantially higher in spring than summer in the Arctic, Commun. Earth Environ., 4, 1–12, https://doi.org/10.1038/s43247-023-00749-x, 2023.

Kanji, Z. A., Welti, A., Corbin, J. C., and Mensah, A. A.: Black Carbon Particles Do Not Matter for Immersion Mode Ice Nucleation, Geophys. Res. Lett., 47, e2019GL086764, https://doi.org/10.1029/2019GL086764, 2020.

Knudsen, E. M., Heinold, B., Dahlke, S., Bozem, H., Crewell, S., Gorodetskaya, I. V., Heygster, G., Kunkel, D., Maturilli, M., Mech, M., Viceto, C., Rinke, A., Schmithüsen, H., Ehrlich, A., Macke, A., Lüpkes, C., and Wendisch, M.: Meteorological conditions during the ACLOUD/PASCAL field campaign near Svalbard in early summer 2017, Atmos. Chem. Phys., 18, 17995–18022, https://doi.org/10.5194/acp-18-17995-2018, 2018.

Kodros, J. K., Hanna, S. J., Bertram, A. K., Leaitch, W. R., Schulz, H., Herber, A. B., Zanatta, M., Burkart, J., Willis, M. D., Abbatt, J. P. D., and Pierce, J. R.: Size-resolved mixing state of black carbon in the Canadian high Arctic and implications for simulated direct radiative effect, Atmos. Chem. Phys., 18, 11345–11361, https://doi.org/10.5194/acp-18-11345-2018, 2018.

Korolev, A., McFarquhar, G., Field, P. R., Franklin, C., Lawson, P., Wang, Z., Williams, E., Abel, S. J., Axisa, D., Borrmann, S., Crosier, J., Fugal, J., Krämer, M., Lohmann, U., Schlenczek, O., Schnaiter, M., and Wendisch, M.: Mixed-Phase Clouds: Progress and Challenges, Meteorol. Monogr., 58, 5.1–5.50, https://doi.org/10.1175/AMSMONOGRAPHS-D-17-0001.1, 2017.

Kupc, A., Williamson, C., Wagner, N. L., Richardson, M., and Brock, C. A.: Modification, calibration, and performance of the Ultra-High Sensitivity Aerosol Spectrometer for particle size distribution and volatility measurements during the Atmospheric Tomography Mission (ATom) airborne campaign, Atmos. Meas. Tech., 11, 369–383, https://doi.org/10.5194/amt-11-369-2018, 2018.

Kupiszewski, P., Zanatta, M., Mertes, S., Vochezer, P., Lloyd, G., Schneider, J., Schenk, L., Schnaiter, M., Baltensperger, U., Weingartner, E., and Gysel, M.: Ice residual properties in mixed-phase clouds at the high-alpine Jungfraujoch site, J. Geophys. Res.-Atmos., 121, 2016JD024894, https://doi.org/10.1002/2016JD024894, 2016.

Laborde, M., Schnaiter, M., Linke, C., Saathoff, H., Naumann, K.-H., Möhler, O., Berlenz, S., Wagner, U., Taylor, J. W., Liu, D., Flynn, M., Allan, J. D., Coe, H., Heimerl, K., Dahlkötter, F., Weinzierl, B., Wollny, A. G., Zanatta, M., Cozic, J., Laj, P., Hitzenberger, R., Schwarz, J. P., and Gysel, M.: Single Particle Soot Photometer intercomparison at the AIDA chamber, Atmos. Meas. Tech., 5, 3077–3097, https://doi.org/10.5194/amt-5-3077-2012, 2012.

Laborde, M., Crippa, M., Tritscher, T., Jurányi, Z., Decarlo, P. F., Temime-Roussel, B., Marchand, N., Eckhardt, S., Stohl, A., Baltensperger, U., Prévôt, A. S. H., Weingartner, E., and Gysel, M.: Black carbon physical properties and mixing state in the European megacity Paris, Atmos. Chem. Phys., 13, 5831–5856, https://doi.org/10.5194/acp-13-5831-2013, 2013.

Leaitch, W. R., Korolev, A., Aliabadi, A. A., Burkart, J., Willis, M. D., Abbatt, J. P. D., Bozem, H., Hoor, P., Köllner, F., Schneider, J., Herber, A., Konrad, C., and Brauner, R.: Effects of 20–100 nm particles on liquid clouds in the clean summertime Arctic, Atmos. Chem. Phys., 16, 11107–11124, https://doi.org/10.5194/acp-16-11107-2016, 2016.

Lubin, D. and Vogelmann, A. M.: A climatologically significant aerosol longwave indirect effect in the Arctic, Nature, 439, 453–456, https://doi.org/10.1038/nature04449, 2006.

Mahmood, R., von Salzen, K., Flanner, M., Sand, M., Langner, J., Wang, H., and Huang, L.: Seasonality of global and Arctic black carbon processes in the Arctic Monitoring and Assessment Programme models, J. Geophys. Res.-Atmos., 121, 2016JD024849, https://doi.org/10.1002/2016JD024849, 2016.

McFarquhar, G. M., Ghan, S., Verlinde, J., Korolev, A., Strapp, J. W., Schmid, B., Tomlinson, J. M., Wolde, M., Brooks, S. D., Cziczo, D., Dubey, M. K., Fan, J., Flynn, C., Gultepe, I., Hubbe, J., Gilles, M. K., Laskin, A., Lawson, P., Leaitch, W. R., Liu, P., Liu, X., Lubin, D., Mazzoleni, C., Macdonald, A.-M., Moffet, R. C., Morrison, H., Ovchinnikov, M., Shupe, M. D., Turner, D. D., Xie, S., Zelenyuk, A., Bae, K., Freer, M., and Glen, A.: Indirect and Semi-direct Aerosol Campaign: The Impact of Arctic Aerosols on Clouds, B. Am. Meteorol. Soc., 92, 183–201, https://doi.org/10.1175/2010BAMS2935.1, 2011.

Mertes, S., Lehmann, K., Nowak, A., Massling, A., and Wiedensohler, A.: Link between aerosol hygroscopic growth and droplet activation observed for hill-capped clouds at connected flow conditions during FEBUKO, Atmos. Environ., 39, 4247–4256, https://doi.org/10.1016/j.atmosenv.2005.02.010, 2005.

Mertes, S., Verheggen, B., Walter, S., Connolly, P., Ebert, M., Schneider, J., Bower, K. N., Cozic, J., Weinbruch, S., Baltensperger, U., and Weingartner, E.: Counterflow Virtual Impactor Based Collection of Small Ice Particles in Mixed-Phase Clouds for the Physico-Chemical Characterization of Tropospheric Ice Nuclei: Sampler Description and First Case Study, Aerosol Sci. Tech., 41, 848–864, https://doi.org/10.1080/02786820701501881, 2007.

Mioche, G., Jourdan, O., Delanoë, J., Gourbeyre, C., Febvre, G., Dupuy, R., Monier, M., Szczap, F., Schwarzenboeck, A., and Gayet, J.-F.: Vertical distribution of microphysical properties of Arctic springtime low-level mixed-phase clouds over the Greenland and Norwegian seas, Atmos. Chem. Phys., 17, 12845–12869, https://doi.org/10.5194/acp-17-12845-2017, 2017.

Mori, T., Kondo, Y., Ohata, S., Zhao, Y., Sinha, P. R., Oshima, N., Matsui, H., Moteki, N., and Koike, M.: Seasonal Variation of Wet Deposition of Black Carbon in Arctic Alaska, J. Geophys. Res.-Atmos., 125, e2019JD032240, https://doi.org/10.1029/2019JD032240, 2020.

Morrison, H., de Boer, G., Feingold, G., Harrington, J., Shupe, M. D., and Sulia, K.: Resilience of persistent Arctic mixed-phase clouds, Nat. Geosci, 5, 11–17, https://doi.org/10.1038/ngeo1332, 2012.

Moteki, N. and Kondo, Y.: Dependence of Laser-Induced Incandescence on Physical Properties of Black Carbon Aerosols: Measurements and Theoretical Interpretation, Aerosol Sci. Tech., 44, 663–675, https://doi.org/10.1080/02786826.2010.484450, 2010.

Moteki, N., Kondo, Y., and Nakamura, S.: Method to measure refractive indices of small nonspherical particles: Application to black carbon particles, J. Aerosol Sci., 41, 513–521, https://doi.org/10.1016/j.jaerosci.2010.02.013, 2010.

Motos, G., Schmale, J., Corbin, J. C., Modini, Rob. L., Karlen, N., Bertò, M., Baltensperger, U., and Gysel-Beer, M.: Cloud droplet activation properties and scavenged fraction of black carbon in liquid-phase clouds at the high-alpine research station Jungfraujoch (3580 m a.s.l.), Atmos. Chem. Phys., 19, 3833–3855, https://doi.org/10.5194/acp-19-3833-2019, 2019a.

Motos, G., Schmale, J., Corbin, J. C., Zanatta, M., Baltensperger, U., and Gysel-Beer, M.: Droplet activation behaviour of atmospheric black carbon particles in fog as a function of their size and mixing state, Atmos. Chem. Phys., 19, 2183–2207, https://doi.org/10.5194/acp-19-2183-2019, 2019b.

Nakoudi, K., Ritter, C., Böckmann, C., Kunkel, D., Eppers, O., Rozanov, V., Mei, L., Pefanis, V., Jäkel, E., Herber, A., Maturilli, M., and Neuber, R.: Does the Intra-Arctic Modification of Long-Range Transported Aerosol Affect the Local Radiative Budget? (A Case Study), Remote Sens., 12, 2112, https://doi.org/10.3390/rs12132112, 2020.

Neuber, R., Schmidt, L. V., Ritter, C., and Mech, M.: Cloud top altitudes observed with airborne lidar during the ACLOUD campaign, PANGAEA [data set], https://doi.org/10.1594/PANGAEA.899962, 2019.

Noone, K. J., Ogren, J. A., Heintzenberg, J., Charlson, R. J., and Covert, D. S.: Design and Calibration of a Counterflow Virtual Impactor for Sampling of Atmospheric Fog and Cloud Droplets, Aerosol Sci. Tech., 8, 235–244, https://doi.org/10.1080/02786828808959186, 1988.

Ogren, J. A., Heintzenberg, J., and Charlson, R. J.: In-situ sampling of clouds with a droplet to aerosol converter, Geophys. Res. Lett., 12, 121–124, https://doi.org/10.1029/GL012i003p00121, 1985.

Ohata, S., Schwarz, J. P., Moteki, N., Koike, M., Takami, A., and Kondo, Y.: Hygroscopicity of materials internally mixed with black carbon measured in Tokyo, J. Geophys. Res.-Atmos., 121, 2015JD024153, https://doi.org/10.1002/2015JD024153, 2016.

Ohata, S., Koike, M., Yoshida, A., Moteki, N., Adachi, K., Oshima, N., Matsui, H., Eppers, O., Bozem, H., Zanatta, M., and Herber, A. B.: Arctic black carbon during PAMARCMiP 2018 and previous aircraft experiments in spring, Atmos. Chem. Phys., 21, 15861–15881, https://doi.org/10.5194/acp-21-15861-2021, 2021.

Oshima, N., Yukimoto, S., Deushi, M., Koshiro, T., Kawai, H., Tanaka, T. Y., and Yoshida, K.: Global and Arctic effective radiative forcing of anthropogenic gases and aerosols in MRI-ESM2.0, Prog. Earth Planet. Sci., 7, 38, https://doi.org/10.1186/s40645-020-00348-w, 2020.

Petzold, A., Onasch, T., Kebabian, P., and Freedman, A.: Intercomparison of a Cavity Attenuated Phase Shift-based extinction monitor (CAPS PMex) with an integrating nephelometer and a filter-based absorption monitor, Atmos. Meas. Tech., 6, 1141–1151, https://doi.org/10.5194/amt-6-1141-2013, 2013.

Quinn, P. K., Stohl, A., Arnold, S., Baklanov, A., Berntsen, T. K., Christensen, J. H., Eckhardt, S., Flanner, M., Klimont, Z., Korsholm, U. S., Kupiainen, K., Langner, J., Law, K., Monks, S., von Salzen, K., Sand, M., Schmale, J., and Vestreng, V.: AMAP Assessment 2015: Black carbon and ozone as Arctic climate forcers, Arctic Monitoring and Assessment Programme (AMAP), Oslo, Norway, vii + 116 pp., ISBN 978-82-7971-092-9, 2015.

Raatikainen, T., Brus, D., Hyvärinen, A.-P., Svensson, J., Asmi, E., and Lihavainen, H.: Black carbon concentrations and mixing state in the Finnish Arctic, Atmos. Chem. Phys., 15, 10057–10070, https://doi.org/10.5194/acp-15-10057-2015, 2015.

Roiger, A., Thomas, J.-L., Schlager, H., Law, K. S., Kim, J., Schäfler, A., Weinzierl, B., Dahlkötter, F., Krisch, I., Marelle, L., Minikin, A., Raut, J.-C., Reiter, A., Rose, M., Scheibe, M., Stock, P., Baumann, R., Bouarar, I., Clerbaux, C., George, M., Onishi, T., and Flemming, J.: Quantifying Emerging Local Anthropogenic Emissions in the Arctic Region: The ACCESS Aircraft Campaign Experiment, B. Am. Meteorol. Soc., 96, 441–460, https://doi.org/10.1175/BAMS-D-13-00169.1, 2015.

Samset, B. H., Myhre, G., Schulz, M., Balkanski, Y., Bauer, S., Berntsen, T. K., Bian, H., Bellouin, N., Diehl, T., Easter, R. C., Ghan, S. J., Iversen, T., Kinne, S., Kirkevåg, A., Lamarque, J.-F., Lin, G., Liu, X., Penner, J. E., Seland, Ø., Skeie, R. B., Stier, P., Takemura, T., Tsigaridis, K., and Zhang, K.: Black carbon vertical profiles strongly affect its radiative forcing uncertainty, Atmos. Chem. Phys., 13, 2423–2434, https://doi.org/10.5194/acp-13-2423-2013, 2013.

Samset, B. H., Stjern, C. W., Andrews, E., Kahn, R. A., Myhre, G., Schulz, M., and Schuster, G. L.: Aerosol Absorption: Progress Towards Global and Regional Constraints, Curr. Clim. Change Rep., 4, 65–83, https://doi.org/10.1007/s40641-018-0091-4, 2018.

Sand, M., Berntsen, T. K., Kay, J. E., Lamarque, J. F., Seland, Ø., and Kirkevåg, A.: The Arctic response to remote and local forcing of black carbon, Atmos. Chem. Phys., 13, 211–224, https://doi.org/10.5194/acp-13-211-2013, 2013.

Schnaiter, M. and Järvinen, E.: SID-3 1Hz size distribution of cloud particles during the ACLOUD campaign in 2017, PANGAEA, https://doi.org/10.1594/PANGAEA.900261, 2019.

Schroder, J. C., Hanna, S. J., Modini, R. L., Corrigan, A. L., Kreidenwies, S. M., Macdonald, A. M., Noone, K. J., Russell, L. M., Leaitch, W. R., and Bertram, A. K.: Size-resolved observations of refractory black carbon particles in cloud droplets at a marine boundary layer site, Atmos. Chem. Phys., 15, 1367–1383, https://doi.org/10.5194/acp-15-1367-2015, 2015.

Schulz, H., Zanatta, M., Bozem, H., Leaitch, W. R., Herber, A. B., Burkart, J., Willis, M. D., Kunkel, D., Hoor, P. M., Abbatt, J. P. D., and Gerdes, R.: High Arctic aircraft measurements characterising black carbon vertical variability in spring and summer, Atmos. Chem. Phys., 19, 2361–2384, https://doi.org/10.5194/acp-19-2361-2019, 2019.

Schwarz, J. P., Gao, R. S., Fahey, D. W., Thomson, D. S., Watts, L. A., Wilson, J. C., Reeves, J. M., Darbeheshti, M., Baumgardner, D. G., Kok, G. L., Chung, S. H., Schulz, M., Hendricks, J., Lauer, A., Kärcher, B., Slowik, J. G., Rosenlof, K. H., Thompson, T. L., Langford, A. O., Loewenstein, M., and Aikin, K. C.: Single-particle measurements of midlatitude black carbon and light-scattering aerosols from the boundary layer to the lower stratosphere, J. Geophys. Res.-Atmos., 111, D16207, https://doi.org/10.1029/2006JD007076, 2006.

Schwarz, J. P., Samset, B. H., Perring, A. E., Spackman, J. R., Gao, R. S., Stier, P., Schulz, M., Moore, F. L., Ray, E. A., and Fahey, D. W.: Global-scale seasonally resolved black carbon vertical profiles over the Pacific, Geophys. Res. Lett., 40, 2013GL057775, https://doi.org/10.1002/2013GL057775, 2013.

Schwarz, J. P., Perring, A. E., Markovic, M. Z., Gao, R. S., Ohata, S., Langridge, J., Law, D., McLaughlin, R., and Fahey, D. W.: Technique and theoretical approach for quantifying the hygroscopicity of black-carbon-containing aerosol using a single particle soot photometer, J. Aerosol Sci., 81, 110–126, https://doi.org/10.1016/j.jaerosci.2014.11.009, 2015.

Sedlar, J., Shupe, M. D., and Tjernström, M.: On the Relationship between Thermodynamic Structure and Cloud Top, and Its Climate Significance in the Arctic, J. Climate, 25, 2374–2393, https://doi.org/10.1175/JCLI-D-11-00186.1, 2011.

Shupe, M. D. and Intrieri, J. M.: Cloud Radiative Forcing of the Arctic Surface: The Influence of Cloud Properties, Surface Albedo, and Solar Zenith Angle, J. Climate, 17, 616–628, https://doi.org/10.1175/1520-0442(2004)017<0616:CRFOTA>2.0.CO;2, 2004.

Solomon, A., Feingold, G., and Shupe, M. D.: The role of ice nuclei recycling in the maintenance of cloud ice in Arctic mixed-phase stratocumulus, Atmos. Chem. Phys., 15, 10631–10643, https://doi.org/10.5194/acp-15-10631-2015, 2015.

Stachlewska, I. S.: Investigation of tropospheric arctic aerosol and mixed-phase clouds using airborne lidar technique, Universität Potsdam, 2005.

Stachlewska, I. S., Neuber, R., Lampert, A., Ritter, C., and Wehrle, G.: AMALi – the Airborne Mobile Aerosol Lidar for Arctic research, Atmos. Chem. Phys., 10, 2947–2963, https://doi.org/10.5194/acp-10-2947-2010, 2010.

Stephens, M., Turner, N., and Sandberg, J.: Particle identification by laser-induced incandescence in a solid-state laser cavity, Appl. Optics, 42, 3726–3736, https://doi.org/10.1364/AO.42.003726, 2003.

Taketani, F., Miyakawa, T., Takashima, H., Komazaki, Y., Kanaya, Y., Taketani, F., Miyakawa, T., Inoue, J., Kanaya, Y., Takashima, H., Pan, X., and Inoue, J.: Ship-borne observations of atmospheric black carbon aerosol particles over the Arctic Ocean, Bering Sea, and North Pacific Ocean during September 2014, J. Geophys. Res.-Atmos., 121, 2015JD023648, https://doi.org/10.1002/2015JD023648, 2016.

Tørseth, K., Andrews, E., Asmi, E., Eleftheriadis, K., Fiebig, M., Herber, A., Huang, L., Kylling, A., Lupi, A., Massling, A., Mazzola, M., Nøjgaard, J. K., Popovicheva, O., Schichtel, B., Schmale, J., Sharma, S., Skov, H., Stebel, K., Vasel, B., Vitale, V., Whaley, C., Yttri, K. E., and Zanatta, M.: Review of Observation Capacities and Data Availability for Black Carbon in the Arctic Region:EU Action on Black Carbon inthe Arctic – Technical Report 1, 2019.

Vochezer, P., Järvinen, E., Wagner, R., Kupiszewski, P., Leisner, T., and Schnaiter, M.: In situ characterization of mixed phase clouds using the Small Ice Detector and the Particle Phase Discriminator, Atmos. Meas. Tech., 9, 159–177, https://doi.org/10.5194/amt-9-159-2016, 2016.

Wendisch, M., Macke, A., Ehrlich, A., Lüpkes, C., Mech, M., Chechin, D., Dethloff, K., Velasco, C. B., Bozem, H., Brückner, M., Clemen, H.-C., Crewell, S., Donth, T., Dupuy, R., Ebell, K., Egerer, U., Engelmann, R., Engler, C., Eppers, O., Gehrmann, M., Gong, X., Gottschalk, M., Gourbeyre, C., Griesche, H., Hartmann, J., Hartmann, M., Heinold, B., Herber, A., Herrmann, H., Heygster, G., Hoor, P., Jafariserajehlou, S., Jäkel, E., Järvinen, E., Jourdan, O., Kästner, U., Kecorius, S., Knudsen, E. M., Köllner, F., Kretzschmar, J., Lelli, L., Leroy, D., Maturilli, M., Mei, L.,

Mertes, S., Mioche, G., Neuber, R., Nicolaus, M., Nomokonova, T., Notholt, J., Palm, M., van Pinxteren, M., Quaas, J., Richter, P., Ruiz-Donoso, E., Schäfer, M., Schmieder, K., Schnaiter, M., Schneider, J., Schwarzenböck, A., Seifert, P., Shupe, M. D., Siebert, H., Spreen, G., Stapf, J., Stratmann, F., Vogl, T., Welti, A., Wex, H., Wiedensohler, A., Zanatta, M., and Zeppenfeld, S.: The Arctic Cloud Puzzle: Using ACLOUD/PASCAL Multiplatform Observations to Unravel the Role of Clouds and Aerosol Particles in Arctic Amplification, B. Am. Meteorol. Soc., 100, 841–871, https://doi.org/10.1175/BAMS-D-18-0072.1, 2018.

Wendisch, M., Brückner, M., Crewell, S., Ehrlich, A., Notholt, J., Lüpkes, C., Macke, A., Burrows, J. P., Rinke, A., Quaas, J., Maturilli, M., Schemann, V., Shupe, M. D., Akansu, E. F., Barrientos-Velasco, C., Bärfuss, K., Blechschmidt, A.-M., Block, K., Bougoudis, I., Bozem, H., Böckmann, C., Bracher, A., Bresson, H., Bretschneider, L., Buschmann, M., Chechin, D. G., Chylik, J., Dahlke, S., Deneke, H., Dethloff, K., Donth, T., Dorn, W., Dupuy, R., Ebell, K., Egerer, U., Engelmann, R., Eppers, O., Gerdes, R., Gierens, R., Gorodetskaya, I. V., Gottschalk, M., Griesche, H., Gryanik, V. M., Handorf, D., Harm-Altstädter, B., Hartmann, J., Hartmann, M., Heinold, B., Herber, A., Herrmann, H., Heygster, G., Höschel, I., Hofmann, Z., Hölemann, J., Hünerbein, A., Jafariserajehlou, S., Jäkel, E., Jacobi, C., Janout, M., Jansen, F., Jourdan, O., Jurányi, Z., Kalesse-Los, H., Kanzow, T., Käthner, R., Kliesch, L. L., Klingebiel, M., Knudsen, E. M., Kovács, T., Körtke, W., Krampe, D., Kretzschmar, J., Kreyling, D., Kulla, B., Kunkel, D., Lampert, A., Lauer, M., Lelli, L., Lerber, A. von, Linke, O., Löhnert, U., Lonardi, M., Losa, S. N., Losch, M., Maahn, M., Mech, M., Mei, L., Mertes, S., Metzner, E., Mewes, D., Michaelis, J., Mioche, G., Moser, M., Nakoudi, K., Neggers, R., Neuber, R., Nomokonova, T., Oelker, J., Papakonstantinou-Presvelou, I., Pätzold, F., Pefanis, V., Pohl, C., van Pinxteren, M., Radovan, A., Rhein, M., Rex, M., Richter, A., Risse, N., Ritter, C., Rostosky, P., Rozanov, V. V., Donoso, E. R., Garfias, P. S., Salzmann, M., Schacht, J., Schäfer, M., Schneider, J., Schnierstein, N., Seifert, P., Seo, S., Siebert, H., Soppa, M. A., Spreen, G., Stachlewska, I. S., Stapf, J., Stratmann, F., Tegen, I., Viceto, C., Voigt, C., Vountas, M., Walbröl, A., Walter, M., Wehner, B., Wex, H., Willmes, S., Zanatta, M., and Zeppenfeld, S.: Atmospheric and Surface Processes, and Feedback Mechanisms Determining Arctic Amplification: A Review of First Results and Prospects of the (AC)3 Project, B. Am. Meteorol. Soc., 1, E208–E242, https://doi.org/10.1175/BAMS-D-21-0218.1, 2022.

Wesche, C., Steinhage, D., and Nixdorf, U.: Polar aircraft Polar5 and Polar6 operated by the Alfred Wegener Institute, J. Large-Scale Res. Facil. JLSRF, 2, A87, https://doi.org/10.17815/jlsrf-2-153, 2016.

Whaley, C. H., Mahmood, R., von Salzen, K., Winter, B., Eckhardt, S., Arnold, S., Beagley, S., Becagli, S., Chien, R.-Y., Christensen, J., Damani, S. M., Dong, X., Eleftheriadis, K., Evangeliou, N., Faluvegi, G., Flanner, M., Fu, J. S., Gauss, M., Giardi, F., Gong, W., Hjorth, J. L., Huang, L., Im, U., Kanaya, Y., Krishnan, S., Klimont, Z., Kühn, T., Langner, J., Law, K. S., Marelle, L., Massling, A., Olivié, D., Onishi, T., Oshima, N., Peng, Y., Plummer, D. A., Popovicheva, O., Pozzoli, L., Raut, J.-C., Sand, M., Saunders, L. N., Schmale, J., Sharma, S., Skeie, R. B., Skov, H., Taketani, F., Thomas, M. A., Traversi, R., Tsigaridis, K., Tsyro, S., Turnock, S., Vitale, V., Walker, K. A., Wang, M.,

Watson-Parris, D., and Weiss-Gibbons, T.: Model evaluation of short-lived climate forcers for the Arctic Monitoring and Assessment Programme: a multi-species, multi-model study, Atmos. Chem. Phys., 22, 5775–5828, https://doi.org/10.5194/acp-22-5775-2022, 2022.

Xu, J.-W., Martin, R. V., Morrow, A., Sharma, S., Huang, L., Leaitch, W. R., Burkart, J., Schulz, H., Zanatta, M., Willis, M. D., Henze, D. K., Lee, C. J., Herber, A. B., and Abbatt, J. P. D.: Source attribution of Arctic black carbon constrained by aircraft and surface measurements, Atmos. Chem. Phys., 17, 11971–11989, https://doi.org/10.5194/acp-17-11971-2017, 2017.

Yoshida, A., Moteki, N., Ohata, S., Mori, T., Tada, R., Dagsson-Waldhauserová, P., and Kondo, Y.: Detection of light-absorbing iron oxide particles using a modified single-particle soot photometer, Aerosol Sci. Tech., 50, 1–4, https://doi.org/10.1080/02786826.2016.1146402, 2016.

Yoshida, A., Moteki, N., Ohata, S., Mori, T., Koike, M., Kondo, Y., Matsui, H., Oshima, N., Takami, A., and Kita, K.: Abundances and Microphysical Properties of Light-Absorbing Iron Oxide and Black Carbon Aerosols Over East Asia and the Arctic, J. Geophys. Res.-Atmos., 125, e2019JD032301, https://doi.org/10.1029/2019JD032301, 2020.

Yuan, J., Modini, R. L., Zanatta, M., Herber, A. B., Müller, T., Wehner, B., Poulain, L., Tuch, T., Baltensperger, U., and Gysel-Beer, M.: Variability in the mass absorption cross section of black carbon (BC) aerosols is driven by BC internal mixing state at a central European background site (Melpitz, Germany) in winter, Atmos. Chem. Phys., 21, 635–655, https://doi.org/10.5194/acp-21-635-2021, 2021.

Zanatta, M. and Herber, A.: Aircraft measurements of aerosol size distribution in the Arctic during the ACLOUD campaign 2017, PANGAEA [data set], https://doi.org/10.1594/PANGAEA.900341, 2019a.

Zanatta, M. and Herber, A.: Aircraft measurements of refractory black carbon in the Arctic during the ACLOUD campaign 2017, PANGAEA [data set], https://doi.org/10.1594/PANGAEA.899937, 2019b.

Zanatta, M., Laj, P., Gysel, M., Baltensperger, U., Vratolis, S., Eleftheriadis, K., Kondo, Y., Dubuisson, P., Winiarek, V., Kazadzis, S., Tunved, P., and Jacobi, H.-W.: Effects of mixing state on optical and radiative properties of black carbon in the European Arctic, Atmos. Chem. Phys., 18, 14037–14057, https://doi.org/10.5194/acp-18-14037-2018, 2018.

Zanatta, M., Bozem, H., Köllner, F., Schneider, J., Kunkel, D., Hoor, P., Faria, J. de, Petzold, A., Bundke, U., Hayden, K., Staebler, R. M., Schulz, H., and Herber, A. B.: Airborne survey of trace gases and aerosols over the Southern Baltic Sea: from clean marine boundary layer to shipping corridor effect, Tellus B, 72, 1–24, https://doi.org/10.1080/16000889.2019.1695349, 2020.